Eindhoven University of Technology

MASTER

Numerical simulation of the advection of passive tracers in 2D flows

van Oijen, J.A.

Award date:
1996

Link to publication

Technische Universiteit **tu** Eindhoven

Vakgroep Transportfysica
Faculteit Technische
Natuurkunde
Gebouw W&S
Postbus 513
5600 MB Eindhoven

Titel: **Numerical Simulation of the Advection
of Passive Tracers in 2D Flows**

Auteur: J.A. van Oijen

Verslagnummer: R–1413–A
Datum: December 1996

Werkeenheid: Werveldynamica
Begeleiders: dr. H.J.H. Clercx
prof. dr. ir. G.J.F. van Heijst

Abstract

The transport properties of 2D flows are relevant to many branches of fluid dynamics. The mixing properties of, for instance, geophysical and industrial flows have received a lot of attention recently.

In order to study the evolution of passive tracers in 2D flows two numerical algorithms have been developed. In the first method, which is based on the Eulerian approach, the advection-diffusion equation for a passive scalar is solved using a pseudospectral method. The time-discretization yields a Helmholtz equation with homogeneous Neumann boundary conditions, which is solved using a Chebyshev tau method. The second method consists of following a large amount of particles and is referred to as the Lagrangian approach. Both methods have been implemented in a spectral solver for the Navier-Stokes equations in the velocity-vorticity formulation.

In order to test the numerical algorithms several simulations are performed. Simulations of natural convection in a square cavity are performed for Rayleigh numbers as high as 10^8 and are used to test the implementation of the Eulerian approach. The results are in excellent agreement with benchmark data from the literature. The evolution of a tracer cloud during spin-up has been simulated in order to estimate the accuracy of the numerical schemes. The results of these simulations appeared to be very dependent on the accuracy of the velocity field. As an example of the application of the developed methods we have simulated the dispersion of a passive tracer in a linear array of vortices. The dispersion of the tracer in such a cellular flow appeared to be a hypodiffusive process, where the variance of the tracer cloud increases in time according to a power law with an exponent close to 0.5.

Contents

Chapter 1

Introduction

The study of two-dimensional (2D) flows has received an important impetus from increased interest in the dynamics and advection properties of geophysical flow systems. With the advent of satellite imagery it became clear that long-lived coherent vortex structures are abundant in the Earth's atmosphere and oceans. Well-known examples of rather persistent, coherent oceanic vortex structures are the Gulf Stream rings that are pinched of from the unstable, meandering current they are named after. In the atmosphere, the high and the low pressure regions are in fact huge vortices that govern to a large extent our weather. Also in atmospheres of other planets large vortices have been observed to exist: the best known examples are probably Jupiter's Great Red Spot (first observed by Hooke, more than 300 years ago) and the Great Dark Spot on Neptune.

The emergence and persistence of these vortex structures are the result of a remarkable property of 2D flows: in contrast to their three-dimensional counterparts, these flows are characterized by the so-called inverse energy cascade, according to which kinetic energy shows a spectral flux to the larger scales of motion. Phenomenologically, this intriguing property — now commonly referred to as self-organization — results in the formation of larger, organized coherent flow structures.

In oceans and planetary atmospheres the background rotation and density stratification, associated with both temperature and salinity gradients, provide the required dynamical constraints to make the large-scale geophysical flows to good approximation two-dimensional. In addition, the geometrical constraint (atmospheres and oceans are in fact thin shells covering the surface of our spherical planet) provides another two-dimensionalization mechanism. Two-dimensionality can also be established in other ways, for example by external magnetic forces or by enclosing the flow in an essentially two-dimensional domain. Such situations are met in magneto-hydrodynamic flows, in plasmas, in accretion disks of neutron stars, and also in soap films. It must be clear that understanding processes in 2D flows is not only relevant to geophysical fluid dynamics, but also to other fields of physics, such as plasma physics and astrophysics.

Chaotic advection properties of 2D flows are relevant to many branches of fluid dynamics. Examples are enhancement of stirring efficiency by chaotic advection (see Aref [1]), the mixing properties

of geophysical flows (see Pierrehumbert [2]), chaotic advection and anomalous diffusion in Rayleigh-Bénard convection (see Solomon & Gollub [3]), and many others, including industrial flow problems. The chaotic transport properties of these flows are generally studied in experiments by following added or naturally available passive tracers, i.e. tracers which have no dynamical influence on the advecting velocity field. In experiments small solid particles or dye can serve as passive tracers. In Nature temperature, salt, but also pollutants in the atmosphere and the oceans may act as passive tracers.

At the Fluid Dynamics Laboratory of the Department of Physics (quasi-) two-dimensional flows are examined in a combined experimental, numerical and theoretical approach. No other field of fluid dynamics has shown a recent increase in importance comparable to that of numerical methods, nor has any other field developed as rapidly. Of course, the main reason for this evolution is the development of computers, from the microcomputer to the Cray, and we see no end of it. Most of the numerical simulation techniques have their own merits and are applied to specific model problems. Due to their superior convergence properties, spectral methods are successfully used for problems which demand high-resolution techniques. A spectral solver for the Navier-Stokes equations in the velocity-vorticity formulation for flows with two nonperiodic directions has been developed by Clercx [4].

The main goal of the research presented in this report is the development and investigation of numerical algorithms for the simulation of advection of passive tracers in 2D flows. Two different methods are implemented in the spectral solver developed by Clercx. In the first method the advection-diffusion equation for a continuous tracer distribution is solved using a pseudospectral method. This Eulerian approach is seldom used and only a few studies appeared on mixing using this method (see, for example, Richards, Jia & Rogers [5]). The second method consists of following a large amount of particles. For the investigation of chaotic advection and mixing this Lagrangian approach is commonly used (see, for instance, [1–3]).

In order to gain some insight in the accuracy of the numerical algorithms, several simulations have been performed. A popular test-problem for high-accuracy schemes is natural convection in a square cavity. This is not only a test for the Navier-Stokes solver, but also for the implementation of the Eulerian approach. The results of the simulations can be compared with data from the literature. Another test for the algorithms is the simulation of the evolution of a passive tracer distribution during spin-up. A third problem, the dispersion of a passive tracer in a linear array of vortices, is an application of the developed methods. Note that a detailed analysis of the transport properties of these flows is beyond the scope of this report, and will be reported elsewhere.

The further organization of this report is as follows. In Chapter 2, the solution procedure of the 2D Navier-Stokes equations is described. Two methods for the simulation of the evolution of a passive tracer distribution are presented in Chapter 3. In Chapter 4, we discuss the results of the simulations. Finally, the main conclusions are given in Chapter 5.

Chapter 2

2D Navier-Stokes Equations

This chapter is devoted to the solution procedure of the 2D Navier-Stokes equations. A pseudospectral method concerning the Navier-Stokes equations in velocity-vorticity formulation for nonperiodic geometries, has been developed by Clercx [4]. In this chapter we give a review of his approach.

2.1 Velocity-Vorticity Approach

In this work we consider a 2D rectangular domain $\mathcal{D}$ with boundary $\partial \mathcal{D}$. The origin of a Cartesian coordinate frame is placed in the center of the domain and the boundary is described by $x = \pm \frac{1}{2} L_x$ and $y = \pm \frac{1}{2} L_y$ (see Figure 2.1). The flow in this domain is described by the 2D Navier-Stokes equations which consist of the momentum equation and the continuity equation. These equations represent the conservation of momentum and mass, respectively. The vorticity equation is obtained by taking the curl of the momentum equation and using the continuity equation. In dimensionless form the vorticity equation reads

$$\frac{\partial \omega}{\partial t} + (\mathbf{u} \cdot \nabla)\omega = \frac{1}{\text{Re}} \nabla^2 \omega \qquad \text{in } \mathcal{D}, \qquad (2.1)$$
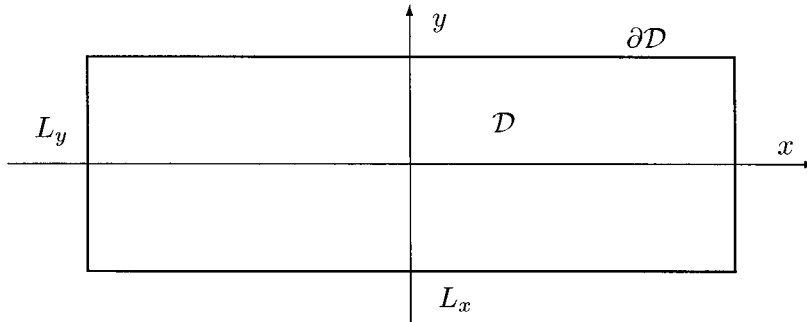

Figure 2.1: Definition of the domain.

where **u** is the dimensionless velocity vector with components (u, v) and $\omega = \frac{\partial v}{\partial x} - \frac{\partial u}{\partial y}$ is the dimensionless vorticity. The vorticity equation has been made dimensionless by introducing the Reynolds number defined as $\text{Re} = \frac{UL}{\nu}$, where U and L are a characteristic velocity and length scale, respectively, and where ν is the kinematic viscosity. In order to solve Eq. (2.1) it is complemented with the definition of the vorticity, the continuity equation and the boundary conditions for the velocity

$$
\begin{array}{llll}
\nabla \times \mathbf{u} & = & \omega \mathbf{k} & \text{in } \mathcal{D}, \\
\nabla \cdot \mathbf{u} & = & 0 & \text{in } \mathcal{D}, \\
\mathbf{u} & = & \mathbf{u}_b & \text{on } \partial \mathcal{D},
\end{array}
\tag{2.2}
$$

where **k** is the unit vector normal to the plane of flow and $\mathbf{u}_b$ is the velocity on the boundary. For a given initial flow field which satisfies the incompressibility constraint and the definition of vorticity, the system can be solved. An extra condition for the flow field is obtained when the continuity equation is integrated over the domain $\mathcal{D}$ and the divergence theorem is applied. This yields

$$
\int_{\partial \mathcal{D}} \mathbf{u} \cdot \mathbf{n} \, d\ell = 0,
\tag{2.3}
$$

where **n** is the unit vector normal to the boundary. This condition implies that the net flow through the boundary equals zero (conservation of mass).

The problem that arises when trying to solve Eqs. (2.1) and (2.2) is that generally the boundary condition for the vorticity is not known. This is due to the fact that the boundary condition for the velocity cannot be reformulated in terms of the vorticity. To tackle this problem several techniques have been developed, varying from approximations as interpolation to more sophisticated techniques like the influence matrix method [6] and the application of vorticity integral conditions [7].

In most studies the definition of the vorticity and the continuity equation are combined in a vector Poisson equation for the velocity. Daube [8] has shown that the formulation of the equations of motion presented by Eqs. (2.1) and (2.2) is mathematically equivalent to the set consisting of the vorticity equation together with the following relations

$$
\begin{array}{llll}
\nabla^2 \mathbf{u} & = & \mathbf{k} \times \nabla \omega & \text{in } \mathcal{D}, \\
\mathbf{u} & = & \mathbf{u}_b & \text{on } \partial \mathcal{D}, \\
\nabla \times \mathbf{u} & = & \omega \mathbf{k} & \text{on } \partial \mathcal{D}.
\end{array}
\tag{2.4}
$$

For a more comprehensive and detailed discussion the reader is referred to Daube [8].

2.2 Time Discretization

The time discretization of the vorticity equation is semi-implicit and second-order accurate. For the advection term an explicit Adams-Bashforth scheme is used and for the diffusive term an implicit Crank-Nicolson scheme. This combination is quite often used in computational fluid dynamics and is generally referred to as the ABCN scheme. Due to the explicit treatment of the advection term, the time-marching scheme has a severe stability condition. To assure stability the dimensionless time step is

restricted to $\Delta t \leq 9/N^2$, with N the cut-off of the Chebyshev expansion [9]. An explicit treatment of the diffusive term would lead to an even more severe stability limit, i.e. $\Delta t \leq C/N^4$ with C some constant. More stable or accurate time schemes like Adams-Moulton or Runge-Kutta methods can be used but are not our main concern.

Since the Adams-Bashforth scheme evaluates the advection term at two previous time levels, it is not self-starting and we need an alternative first time-integration step. A combination of a second-order Runge-Kutta scheme with a Crank-Nicolson scheme for the viscous term has been used to tackle this problem. This time discretization is second-order accurate and needs only one previous time level, but per time step it evaluates an intermediate solution of the vorticity and velocity. A more detailed discussion about this first time step is given by Willemen [10].

Applying the ABCN scheme to the vorticity equation (Eq. (2.1)) yields[1]

$$\frac{\omega^{n+1} - \omega^n}{\Delta t} = -\left[\frac{3}{2}(\mathbf{u} \cdot \nabla)\omega^n - \frac{1}{2}(\mathbf{u} \cdot \nabla)\omega^{n-1}\right] + \frac{1}{\mathrm{Re}}\left[\frac{1}{2}\nabla^2\omega^{n+1} + \frac{1}{2}\nabla^2\omega^n\right].$$

(2.5)

With the introduction of $\lambda = \frac{2\mathrm{Re}}{\Delta t}$ the time discretization of the equations of motion results in

$$
\begin{aligned}
(\nabla^2 - \lambda)\omega^{n+1} &= S^{n,n-1} & &\text{in } \mathcal{D}, \\
\nabla^2 \mathbf{u}^{n+1} &= \mathbf{k} \times \nabla\omega^{n+1} & &\text{in } \mathcal{D}, \\
\mathbf{u}^{n+1} &= \mathbf{u}_\mathrm{b}^{n+1} & &\text{on } \partial\mathcal{D}, \\
\nabla \times \mathbf{u}^{n+1} &= \omega^{n+1}\mathbf{k} & &\text{on } \partial\mathcal{D},
\end{aligned}
$$

(2.6)

where $S^{n,n-1}$ includes all explicitly evaluated terms

$$S^{n,n-1} = -(\nabla^2 + \lambda)\omega^n + \mathrm{Re}\left[3(\mathbf{u} \cdot \nabla)\omega^n - (\mathbf{u} \cdot \nabla)\omega^{n-1}\right].$$

(2.7)

Due to the time discretization the set of Eqs. (2.1) and (2.4) has been reduced to a Helmholtz equation for the vorticity and a vector Poisson equation for the velocity. This linear set of elliptic differential equations (2.6) can be solved when the boundary conditions are known. From here the reference to the time level will be omitted.

2.3 Spatial Approximation

For now we are interested in the flow in a rectangular domain with no-slip boundary conditions. For large Reynolds numbers there will appear thin boundary layers with thickness $\mathcal{O}(1/\sqrt{\mathrm{Re}})$. To approximate these thin layers accurately, a high resolution method is required. A pseudospectral method based on the expansion of the relevant flow parameters in terms of Chebyshev polynomials $T_k(x)$ can satisfy this requirement. The assets of spectral methods are exponential convergence and reduced numerical damping and dispersion.

---

[1]The superscripts denote the time level, i.e. $\omega^{n+1} = \omega((n+1)\Delta t)$.
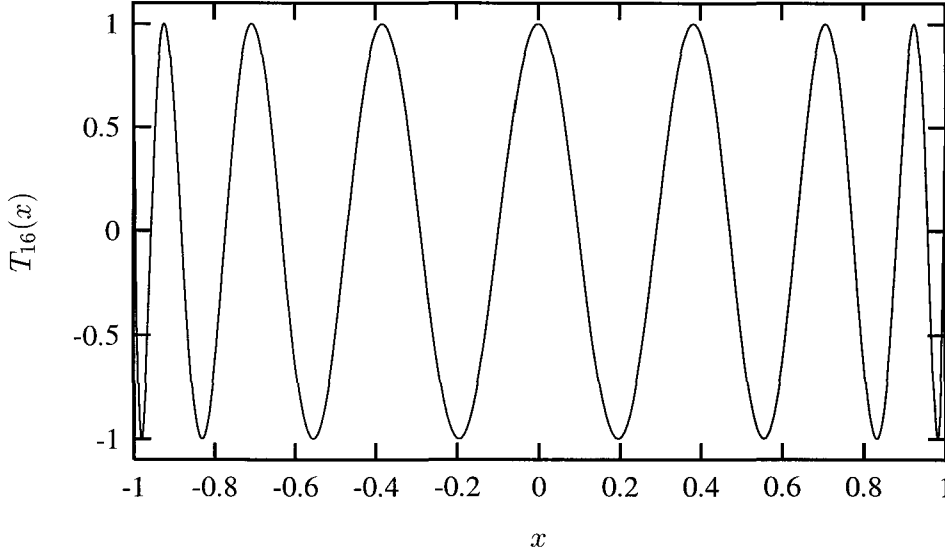
Figure 2.2: Chebyshev polynomial $T_{16}(x)$.

The Chebyshev polynomials can be expressed as

$$T_k(x) = \cos(k\theta) \quad \text{with} \quad \theta = \arccos(x). \tag{2.8}$$

In Figure 2.2 the Chebyshev polynomial $T_{16}(x)$ is shown. The physical domain $\mathcal{D}$ is transformed to the computational domain $[-1, 1] \times [-1, 1]$, since the Chebyshev polynomials are defined inside this range.

Both the vorticity and the velocity are expanded in double truncated series of Chebyshev polynomials, i.e.,

$$\omega(x, y, t) = \sum_{k=0}^{N} \sum_{l=0}^{M} \hat{\omega}_{kl}(t) T_k(x) T_l(y), \tag{2.9}$$

$$\mathbf{u}(x, y, t) = \sum_{k=0}^{N} \sum_{l=0}^{M} \hat{\mathbf{u}}_{kl}(t) T_k(x) T_l(y). \tag{2.10}$$

The expansion coefficients (denoted by the hat) can be obtained using the orthogonality relations for Chebyshev polynomials and a collocation procedure at the Chebyshev-Gauss-Lobatto points. This results in

$$\hat{\omega}_{kl} = \frac{4}{\bar{c}_k \bar{c}_l N M} \sum_{i=0}^{N} \sum_{j=0}^{M} \omega(x_i, y_j, t) T_k(x_i) T_l(y_j), \tag{2.11}$$

where x_i and y_j are the Chebyshev-Gauss-Lobatto points

$$\begin{aligned} x_i &= \cos\left(\frac{i\pi}{N}\right) \quad 0 \le i \le N, \\ y_j &= \cos\left(\frac{j\pi}{M}\right) \quad 0 \le j \le M, \end{aligned} \tag{2.12}$$

and $\bar{c}_i$ is a constant

$$\bar{c}_k = \begin{cases} 1 & 1 \leq k \leq N-1 \\ 2 & k = 0 \text{ or } N \end{cases}. \tag{2.13}$$

The grid points (x_i, y_j) condense near the boundaries (the distance between adjacent grid points near the boundary is $\mathcal{O}(N^{-2})$). Therefore, steep gradients in the flow field near the boundary can easily be resolved.

It is possible to perform the transformation from physical space to spectral space, and vice versa, using a Fast Fourier Transform (FFT) method, because the Chebyshev expansion is, in effect, a cosine sum in terms of the variables $(\arccos(x), \arccos(y))$. This fast transform method is especially important for the evaluation of the nonlinear term. In spectral space the quadratic nonlinear term produces convolution-type sums which can be computed at great costs ($\mathcal{O}(N^2 M^2)$ operations). A more sophisticated procedure has been designed by Orszag [11]. This method consists of the following steps: first are both the velocity and the vorticity transformed to physical space using an FFT method. Then the product is taken in physical space and the result is transformed back to spectral space, again using FFTs. Aliasing errors are eliminated using the padding technique (see, for instance Canuto *et al.* [9]).

Both Helmholtz and Poisson equations are solved in spectral space using the efficient Haidvogel-Zang algorithm [12]. The boundary conditions are imposed by the Lanczos tau method, which consists of dropping the two highest modes of the Chebyshev expansion in favour of the boundary condition. In the Haidvogel-Zang algorithm the elliptic equations are formulated in terms of second-order derivative operators working on the expansion coefficients. One of the operators (e.g., $\frac{\partial^2}{\partial^2 x}$) is diagonalized, which results in a set of decoupled 1D Helmholtz equations. Using the recursion formulas for Chebyshev polynomials, these equations can be simplified and then be solved very efficiently with a modified Thomas algorithm. A more detailed treatment of the Haidvogel-Zang algorithm will be given in Section 3.1.2.

Because of the even-odd properties of the Chebyshev polynomials, it is possible to employ an even-odd decoupling to the complete algorithm. This enhances the efficiency of the algorithm concerning CPU-time and memory requirements.

For a more complete review on spectral methods in fluid dynamics the reader is referred to Canuto *et al.* [9].

2.4 Influence Matrix Method

The time discretization of the vorticity equation yields a linear elliptic partial differential equation, which can be solved when the boundary condition is known. However, this boundary condition is not known *a priori* and has to be evaluated each time step. We have used an influence matrix method to obtain the correct boundary conditions for the vorticity. This method has already been used in previous studies concerning the primitive variable formulation. In this formulation the influence matrix method is used to resolve the lack of boundary conditions for the pressure [6]. (See also Werne [13]

who discusses a minor but important modification.) An implementation of this method for the $(\mathbf{u}, \omega)$ formulation has been presented by Daube [8].

The influence matrix technique is based on the superposition principle for linear equations. The solution of an elliptic problem with unknown boundary condition can be found by considering a superposition of elementary problems with known boundary condition. The solutions of these elementary problems are combined in a self-consistent way satisfying some extra conditions for the total solution. Daube demonstrated that enforcement of the vorticity at the boundary of the domain is sufficient to ensure the definition of the vorticity in the whole domain and the flow being divergence-free. An alternative approach, enforcement of the continuity equation, also gives satisfactory results [4, 8].

Following Daube, we derive the Poisson equation for the velocity field by taking the curl of the definition of the vorticity, $\nabla \times (\nabla \times \mathbf{u})$, subsequently using the vector relation defining the vector Laplacian, $\nabla^2 \mathbf{u} = \nabla(\nabla \cdot \mathbf{u}) - \nabla \times (\nabla \times \mathbf{u})$, and applying the assumption that the velocity field is divergence-free. We now see that there actually exists an infinite number of solutions of the vorticity equation combined with the Poisson equation, for which the vorticity is not necessarily the curl of $\mathbf{u}$, i.e. $\nabla \times \mathbf{u} = \zeta \neq \omega$, and the flow field is not divergence-free. In order to satisfy the definition of the vorticity and to obtain divergence-free velocity fields, we have to enforce the following relation

$$\nabla^2 \mathbf{u} = \nabla(\nabla \cdot \mathbf{u}) + \mathbf{k} \times \nabla \zeta = \mathbf{k} \times \nabla \omega. \tag{2.14}$$

Taking the cross product of (2.14) with $\mathbf{k}$ and the divergence of the resulting equation yields the Laplace equation

$$\nabla^2(\zeta - \omega) = 0 \qquad \text{in } \mathcal{D}. \tag{2.15}$$

The maximum and minimum value of the solution of a Laplace equation will occur on the boundary. Therefore demanding $\zeta = \omega$ on $\partial \mathcal{D}$ is sufficient to satisfy the requirements.

The enforcement of the definition of the vorticity at the boundary is performed by the influence matrix method. Consider the following vorticity and velocity fields

$$\omega = \tilde{\omega} + \sum_{i=1}^{P} \alpha_i \bar{\omega}_i \tag{2.16}$$

and

$$\mathbf{u} = \tilde{\mathbf{u}} + \sum_{i=1}^{P} \alpha_i \bar{\mathbf{u}}_i. \tag{2.17}$$

Here the vorticity and velocity are written as a sum of a particular solution $(\tilde{\omega}, \tilde{\mathbf{u}})$ and a set of complementary solutions $(\bar{\omega}_i, \bar{\mathbf{u}}_i)$. The summation $\sum_{i=1}^{P}$ represents all the points which lie along the boundary excluding the corner points. The particular solution $\tilde{\omega}$ is a solution of the vorticity equation with arbitrary boundary conditions. The most obvious choice is the homogeneous boundary condition. There-

fore the particular solutions $\tilde{\omega}$ and $\tilde{\mathbf{u}}$ are obtained by solving the following problem

$$
\begin{aligned}
(\nabla^2 - \lambda)\tilde{\omega} &= S && \text{in } \mathcal{D}, \\
\tilde{\omega} &= 0 && \text{on } \partial\mathcal{D}, \\
\nabla^2\tilde{\mathbf{u}} &= \mathbf{k} \times \nabla\tilde{\omega} && \text{in } \mathcal{D}, \\
\tilde{\mathbf{u}} &= 0 && \text{on } \partial\mathcal{D}.
\end{aligned}
\tag{2.18}
$$

The complementary solutions $\bar{\omega}_i$ are solutions of the vorticity equation with zero source term and zero boundary condition except at one boundary point, where it equals one. The complementary velocity fields $\bar{\mathbf{u}}_i$ are obtained by solving the Poisson equation. Summarizing, $\bar{\omega}_i$ and $\bar{\mathbf{u}}_i$ are solutions of the following set of equations

$$
\begin{aligned}
(\nabla^2 - \lambda)\bar{\omega}_i &= 0 && \text{in } \mathcal{D}, \\
\bar{\omega}_i(\gamma_j) &= \delta_{ij} && \text{on } \partial\mathcal{D}, \\
\nabla^2\bar{\mathbf{u}}_i &= \mathbf{k} \times \nabla\bar{\omega}_i && \text{in } \mathcal{D}, \\
\bar{\mathbf{u}}_i &= 0 && \text{on } \partial\mathcal{D},
\end{aligned}
\tag{2.19}
$$

where i runs from 1 to P, γ_j are the relevant boundary nodes and δ_{ij} is the Kronecker delta. By demanding $\zeta = \omega$ at the boundary nodes, the coefficients α_i can be obtained:

$$
(\tilde{\zeta} - \tilde{\omega})_j + \sum_{i=1}^{P} \alpha_i(\bar{\zeta}_i - \bar{\omega}_i)_j = 0.
\tag{2.20}
$$

Here are $(\bar{\zeta}_i - \bar{\omega}_i)_j$ the components M_{ji} of the influence matrix $\mathbf{M}$. Since Eq. (2.19) is time independent, the influence matrix can be determined in a preprocessing stage. The inversion is stored and is used to obtain the coefficients α_i which represent the value of the vorticity at the boundary nodes

$$
\alpha_i = -\sum_{i=1}^{P} M_{ij}^{-1}(\tilde{\zeta} - \tilde{\omega})_j.
\tag{2.21}
$$

The vorticity equation and the Poisson equation are now solved again with the correct boundary conditions. This procedure is more economical than storing the complementary solutions to achieve adequate linear combinations.

2.5 Tau-correction

Simulation of the Navier-Stokes equations in the $(\mathbf{u}, \omega)$ formulation using an algorithm as described so far, exhibits enormous numerical instabilities. Although the definition of the vorticity is satisfied within machine accuracy on the boundary, it is not in the interior of the domain. As a consequence the velocity field is not divergence-free. This seems to contradict with the analysis presented by Daube. His analysis is, of course, mathematically correct, but numerically it is not, because of numerical contamination caused by the discrete representation of the equations of motion. In simulations based on the primitive variables approach analogous problems occur, which result in interior divergences as well. However, these divergences do not lead to numerical instabilities.

To correct these interior divergences different techniques have been introduced. One of them is the tau-correction, which can be applied when the differential equations are solved in spectral space. Because of the Lanczos-tau procedure to impose the boundary conditions, the differential equations are not satisfied numerically for the highest frequency modes. A discussion on the tau-correction can be found in the paper by Tuckerman [14].

In order to understand the tau-correction for the $(\mathbf{u}, \omega)$ approach, we first consider the primitive variables case. The time discretized momentum equation reads

$$(\nabla^2 - \lambda)\mathbf{u} - \nabla p = \mathbf{T} + \mathbf{B}, \qquad (2.22)$$

where p is the normalized pressure, λ as before, and $\mathbf{T}$ an anologous expression as Eq. (2.7). The vector $\mathbf{B}$ is a representation of the highest frequency modes and therefore its Chebyshev expansion coefficients $\mathbf{B}_{nm}$ are zero for $n \leq N - 2$ and $m \leq M - 2$. Since the solution procedure of the equation does not involve the highest frequency modes of the source, the solution of Eq. (2.22) is independent of $\mathbf{B}$ [12]. However, the velocity is influenced by $\mathbf{B}$ in an indirect way via the pressure. The pressure follows from the pressure equation, which can be derived by taking the divergence of Eq. (2.22). This yields

$$\nabla^2 p = -\nabla \cdot \mathbf{T} - \nabla \cdot \mathbf{B}. \qquad (2.23)$$

Because differentiation of a Chebyshev polynomial of degree k results in the appearance of Chebyshev polynomials of lower degree, the highest modes of $\mathbf{B}$ contribute to the solution of Eq. (2.23). The lower modes of $\nabla \cdot \mathbf{B}$ act as an extra source term, resulting in a modified pressure field, which, on its part, modifies the velocity field. In order to keep the flow divergence-free, the high frequency modes have to be determined in such a way that Eq. (2.22) is satisfied in a self-consistent way. This implies that after calculation of $\mathbf{u}$ and p, the operation $(\nabla^2 - \lambda)\mathbf{u} - \nabla p - \mathbf{T}$ should exactly be equal to the high frequency modes.

Before returning to the vorticity equation, we first show what causes the breakdown of Daube's theory. Anticipating on a tau-correction technique, the Poisson equation reads

$$\nabla^2 \mathbf{u} = \nabla(\nabla \cdot \mathbf{u}) + \mathbf{k} \times \nabla \zeta = \mathbf{k} \times \nabla \omega + \mathbf{B}^*, \qquad (2.24)$$

where $\mathbf{B}^*$ is again a representation of the high frequency modes, but now with an asterix to avoid confusion with $\mathbf{B}$ in Eq. (2.22). Although $\mathbf{B}^*$ does not affect the velocity field $\mathbf{u}$ itself, it does influence the difference between ζ and ω. This is demonstrated when we follow the procedure as in Section 2.4. We obtain

$$\nabla^2(\zeta - \omega) = -\nabla \cdot (\mathbf{k} \times \mathbf{B}^*), \qquad (2.25)$$

which is obviously not a Laplace equation but a Poisson equation. Because the derivatives of the high frequency modes act as a source, the maximum-principle for Laplace equations is no longer effective. In order to resolve this problem the high frequency modes $\mathbf{B}^*$ should be set equal to zero in a self-consistent way.

The vorticity equation is obtained by taking the curl of the momentum equation (2.22), which yields

$$(\nabla^2 - \lambda)\omega = S + \mathbf{k} \cdot (\nabla \times \mathbf{B}),\tag{2.26}$$

where $S = \mathbf{k} \cdot (\nabla \times \mathbf{T})$ represents the previous time levels. Besides the unknown boundary condition for the vorticity, the high frequency modes $\mathbf{B}$ have to be determined. This should be done in such way that the high frequency modes $\mathbf{B}^*$ in Eq. (2.24) are equal to zero. This can be achieved by introducing another set of complementary solutions, $\bar{\bar{\omega}}_i$ and $\bar{\bar{\mathbf{u}}}_i$. Together with Eqs. (2.16) and (2.17), the vorticity and velocity are now written as

$$\omega = \tilde{\omega} + \sum_{i=1}^{P} \alpha_i \bar{\omega}_i + \sum_{i=1}^{Q} \beta_i \bar{\bar{\omega}}_i\tag{2.27}$$

and

$$\mathbf{u} = \tilde{\mathbf{u}} + \sum_{i=1}^{P} \alpha_i \bar{\mathbf{u}}_i + \sum_{i=1}^{Q} \beta_i \bar{\bar{\mathbf{u}}}_i,\tag{2.28}$$

where $Q = 2N + 2M - 4$ the total number of relevant high frequency modes. This second set of complementary functions are solutions of the following set of equations

$$\begin{aligned}
(\nabla^2 - \lambda)\bar{\bar{\omega}}_i &= \mathbf{k} \cdot (\nabla \times \mathbf{b}_i) & \text{in } \mathcal{D}, \\
\bar{\bar{\omega}}_i &= 0 & \text{on } \partial\mathcal{D}, \\
\nabla^2 \bar{\bar{\mathbf{u}}}_i &= \mathbf{k} \times \nabla\bar{\bar{\omega}}_i & \text{in } \mathcal{D}, \\
\bar{\bar{\mathbf{u}}}_i &= 0 & \text{on } \partial\mathcal{D},
\end{aligned}\tag{2.29}$$

where $\mathbf{b}_i$, with $i = 1, \dots, Q$, are the high frequency modes, which are subsequently set equal to one. The correct combination of the solutions is obtained by simultaneously putting $\nabla \times \mathbf{u} = \omega\mathbf{k}$ at all boundary points and requiring $\mathbf{B}^* = 0$. This yields the following equations for α_i and β_i

$$(\tilde{\zeta} - \tilde{\omega})_j + \sum_{i=1}^{P} \alpha_i(\bar{\zeta}_i - \bar{\omega}_i)_j + \sum_{i=1}^{Q} \beta_i(\bar{\bar{\zeta}}_i - \bar{\bar{\omega}}_i)_j = 0\tag{2.30}$$

and

$$\tilde{\mathbf{B}}_j^* + \left(\sum_{i=1}^{P} \alpha_i \bar{\mathbf{B}}_i^*\right)_j + \left(\sum_{i=1}^{Q} \beta_i \bar{\bar{\mathbf{B}}}_i^*\right)_j = 0,\tag{2.31}$$

where

$$\begin{aligned}
\tilde{\mathbf{B}}^* &= \nabla^2\tilde{\mathbf{u}} - \mathbf{k} \times \nabla\tilde{\omega}, \\
\bar{\mathbf{B}}_i^* &= \nabla^2\bar{\mathbf{u}}_i - \mathbf{k} \times \nabla\bar{\omega}_i & \text{with} \quad i = 1, \dots, P, \\
\bar{\bar{\mathbf{B}}}_i^* &= \nabla^2\bar{\bar{\mathbf{u}}}_i - \mathbf{k} \times \nabla\bar{\bar{\omega}}_i & \text{with} \quad i = 1, \dots, Q,
\end{aligned}\tag{2.32}$$

are the high frequency residuals of the Poisson equation. The influence matrix $\mathbf{M}$ is expanded with terms concerning the tau-correction technique

$$\mathbf{M} = \begin{pmatrix} M_{ji}^{11} & M_{ji}^{12} \\ M_{ji}^{21} & M_{ji}^{22} \end{pmatrix} = \begin{pmatrix} (\bar{\zeta}_i - \bar{\omega}_i)_j & (\bar{\bar{\zeta}}_i - \bar{\bar{\omega}}_i)_j \\ (\bar{\mathbf{B}}_i^*)_j & (\bar{\bar{\mathbf{B}}}_i^*)_j \end{pmatrix}.\tag{2.33}$$

Because this influence matrix is time independent as well, it can be determined in a preprocessing stage. The inversion of $\mathbf{M}$ is stored and is used to obtain the coefficients α_i and β_i

$$\alpha_i = -\sum_{j=1}^{P}(M^{-1})_{ij}^{11}(\tilde{\zeta} - \tilde{\omega})_j - \sum_{j=1}^{Q}(M^{-1})_{ij}^{12}\tilde{\mathbf{U}}_j, \tag{2.34}$$

$$\beta_i = -\sum_{j=1}^{P}(M^{-1})_{ij}^{21}(\tilde{\zeta} - \tilde{\omega})_j - \sum_{j=1}^{Q}(M^{-1})_{ij}^{22}\tilde{\mathbf{U}}_j. \tag{2.35}$$

Now both α_i and β_i are known, and we proceed, as explained in Section 2.4, by determining the vorticity and velocity field by solving Eq. (2.6) with the correct boundary conditions and high frequency modes.

Chapter 3

Passive Tracers

In this chapter we describe two numerical methods which can be used to investigate transport phenomena of passive tracers. The first and the second section are devoted to the Eulerian and the Lagrangian approach, respectively. Some quantities to characterize dispersion are given in the last section.

3.1 Eulerian Approach

This section is devoted to the Eulerian approach of the transport of passive tracers. In this method the tracer is regarded as a continuous scalar field, and it is for that reason sometimes referred to as the continuous model. In order to investigate dispersion of a tracer, this approach has been used in various fields of fluid dynamics, for example, oceanography (e.g., see Richards, Jia & Rogers [5]) and astrophysics (e.g., see Knobloch & Merryfield [15]).

3.1.1 Governing equations

We consider a continuous distribution $c(x, y, t)$ of a passive tracer in the domain $\mathcal{D}$ as described in Section 2.1. The transport of such a passive scalar field in a flow is governed by the advection-diffusion equation

$$\frac{\partial c}{\partial t} + (\mathbf{u} \cdot \nabla)c = \frac{1}{\text{Pe}} \nabla^2 c \qquad \text{in } \mathcal{D}. \tag{3.1}$$

Eq. (3.1) has been made dimensionless by introducing the Peclet number defined as $\text{Pe} = \frac{UL}{\kappa}$, where U and L are a characteristic velocity and length scale, respectively, and where κ is the diffusivity of the tracer. The ratio of diffusion of tracer and of momentum (ν) is given by the Schmidt number defined as $\text{Sc} = \text{Pe}/\text{Re} = \nu/\kappa$. If the scalar c represents a temperature field, then this ratio is referred to as the Prandtl number Pr.

We impose a no-flux boundary condition, which is equivalent to imposing a zero normal gradient

$$\frac{\partial c}{\partial \mathbf{n}} = 0 \qquad \text{on } \partial \mathcal{D}. \tag{3.2}$$

Although Eq. (3.1) is a linear differential equation, exact solutions do not exist for most flows of interest. Therefore the advection-diffusion equation is solved numerically for a given initial concentration field with the velocity obtained as described in Chapter 2. Since the vorticity equation is, in effect, an advection-diffusion equation for ω, the discretization of Eq. (3.1) is performed similarly to the discretization of Eq. (2.1).

Applying the ABCN scheme to the advection-diffusion equation results in the time discretized form

$$(\nabla^2 - \lambda_c)c^{n+1} = S_c^{n,n-1} \qquad \text{in } \mathcal{D}, \qquad (3.3)$$

$$\frac{\partial c^{n+1}}{\partial \mathbf{n}} = 0 \qquad \text{on } \partial\mathcal{D}, \qquad (3.4)$$

where $\lambda_c = \frac{2\text{Pe}}{\Delta t}$, and

$$S_c^{n,n-1} = -(\nabla^2 + \lambda_c)c^n + \text{Pe}\left[3(\mathbf{u} \cdot \nabla)c^n - (\mathbf{u} \cdot \nabla)c^{n-1}\right], \qquad (3.5)$$

an analogous expression as Eq. (2.7).

An influence matrix method to obtain the correct boundary conditions is not needed, since the boundary condition for the concentration is known *a priori*.

The spatial approximation of the concentration field is performed similarly to the discretization of the flow parameters, i.e. the passive scalar is expanded in a double truncated series of Chebyshev polynomials and Eq. (3.3) is solved in spectral space. The advection term in Eq. (3.5) is evaluated pseudospectrally using the procedure designed by Orszag [11].

We can conclude that, due to the time discretization, the advection-diffusion equation is reduced to a Helmholtz equation for the concentration c with homogeneous Neumann boundary conditions.

3.1.2 Helmholtz equation with Neumann boundary condition

Above we have demonstrated that the solution procedure of the advection-diffusion equation consists of solving a Helmholtz equation at each time step. This section concerns the solution of this elliptic partial differential equation with homogeneous Neumann boundary conditions.

Because Eq. (3.3) will be solved in spectral space, the scalar field c is expanded in a double truncated series of Chebyshev polynomials:

$$c(x,y,t) = \sum_{k=0}^{N}\sum_{l=0}^{M} \hat{c}_{kl}(t)T_k(x)T_l(y). \qquad (3.6)$$

Using $\frac{dT_k}{dx}(\pm 1) = (\pm 1)^k k^2$ and the orthogonality relation for Chebyshev polynomials, the boundary

conditions in terms of expansion coefficients are

$$\sum_{k=0}^{N} k^2 \hat{c}_{kl} = 0 \qquad\qquad l = 0, 1, \dots, M, \qquad\qquad (3.7)$$

$$\sum_{k=0}^{N} (-1)^k k^2 \hat{c}_{kl} = 0 \qquad\qquad l = 0, 1, \dots, M, \qquad\qquad (3.8)$$

$$\sum_{l=0}^{M} l^2 \hat{c}_{kl} = 0 \qquad\qquad k = 0, 1, \dots, N, \qquad\qquad (3.9)$$

$$\sum_{l=0}^{M} (-1)^l l^2 \hat{c}_{kl} = 0 \qquad\qquad k = 0, 1, \dots, N. \qquad\qquad (3.10)$$

These boundary conditions are imposed using the Lanczos tau procedure, therefore the Chebyshev tau approximation of Eqs. (3.3) and (3.4) is[1]

$$\hat{c}_{kl}^{(20)} + \hat{c}_{kl}^{(02)} - \lambda \hat{c}_{kl} = \hat{S}_{kl} \qquad\qquad \begin{aligned} k &= 0, 1, \dots, N - 2, \\ l &= 0, 1, \dots, M - 2, \end{aligned} \qquad\qquad (3.11)$$

$$\hat{c}_{Nl} = -\frac{1}{N^2} \sum_{\substack{k=0 \\ k \text{ even}}}^{N-2} k^2 \hat{c}_{kl} \qquad\qquad l = 0, 1, \dots, M, \qquad\qquad (3.12)$$

$$\hat{c}_{N-1,l} = -\frac{1}{(N-1)^2} \sum_{\substack{k=1 \\ k \text{ odd}}}^{N-3} k^2 \hat{c}_{kl} \qquad\qquad l = 0, 1, \dots, M, \qquad\qquad (3.13)$$

$$\hat{c}_{kM} = -\frac{1}{M^2} \sum_{\substack{l=0 \\ l \text{ even}}}^{M-2} l^2 \hat{c}_{kl} \qquad\qquad k = 0, 1, \dots, N, \qquad\qquad (3.14)$$

$$\hat{c}_{n,M-1} = -\frac{1}{(M-1)^2} \sum_{\substack{l=1 \\ l \text{ odd}}}^{M-3} l^2 \hat{c}_{kl} \qquad\qquad k = 0, 1, \dots, N, \qquad\qquad (3.15)$$

where the superscripts (20) and (02) in Eq. (3.11) denote the second derivative with respect to x and y, respectively. The coefficients $\hat{c}_{kl}^{(20)}$ and $\hat{c}_{kl}^{(02)}$ can be expressed as

$$\hat{c}_{kl}^{(20)} = \frac{1}{\bar{c}_k} \sum_{\substack{p=k+2 \\ p+k \text{ even}}}^{N} p(p^2 - k^2) \hat{c}_{pl}, \qquad\qquad (3.16)$$

and

$$\hat{c}_{kl}^{(02)} = \frac{1}{\bar{c}_l} \sum_{\substack{p=l+2 \\ p+l \text{ even}}}^{M} p(p^2 - l^2) \hat{c}_{kp}, \qquad\qquad (3.17)$$

---

[1]The subscripts of λ_c and S_c and the superscripts denoting the time level are omitted.

where $\bar{\bar{c}}_k$ is a constant

$$\bar{\bar{c}}_k = \left\{ \begin{array}{ll} 1 & \text{if } k \geq 1 \\ 2 & \text{if } k = 0 \end{array} \right. . \tag{3.18}$$

Substitution of (3.12) in (3.16) results in the coefficients of the second derivative with incorporated boundary conditions for k even

$$\hat{c}_{kl}^{(20)} = \frac{1}{\bar{\bar{c}}_k} \sum_{\substack{p=k+2 \\ p+k \text{ even}}}^{N-2} p(p^2 - k^2)\hat{c}_{pl} - \frac{1}{\bar{\bar{c}}_k N}(N^2 - k^2) \sum_{\substack{p=0 \\ p \text{ even}}}^{N-2} p^2 \hat{c}_{pl}. \tag{3.19}$$

A similar procedure yields the coefficients for the odd case

$$\hat{c}_{kl}^{(20)} = \sum_{\substack{p=k+2 \\ p+k \text{ even}}}^{N-3} p(p^2 - k^2)\hat{c}_{pl} - \frac{1}{(N-1)}((N-1)^2 - k^2) \sum_{\substack{p=1 \\ p \text{ odd}}}^{N-3} p^2 \hat{c}_{pl}. \tag{3.20}$$

With the introduction of matrix $\mathbf{A}$, which contains the components A_{kp} defined by

$$k, p \text{ even:} \qquad A_{kp} = \left\{ \begin{array}{ll} -\frac{1}{\bar{\bar{c}}_k N}(N^2 - k^2)p^2 & p \leq k \\ \frac{1}{\bar{\bar{c}}_k}p(p^2 - k^2) - \frac{1}{\bar{\bar{c}}_k N}(N^2 - k^2)p^2 & p > k \end{array} \right. , \tag{3.21}$$

$$k, p \text{ odd:} \qquad A_{kp} = \left\{ \begin{array}{ll} -\frac{1}{(N-1)}((N-1)^2 - k^2)p^2 & p \leq k \\ p(p^2 - k^2) - \frac{1}{(N-1)}((N-1)^2 - k^2)p^2 & p > k \end{array} \right. , \tag{3.22}$$

the Helmholtz equation is written in matrix notation

$$\mathbf{AC} + \mathbf{CB} - \lambda \mathbf{C} = \mathbf{S}, \tag{3.23}$$

where $\mathbf{C}$ is a $(N - 1) \times (M - 1)$ matrix, which consists of $\hat{c}_{kl}$ for $k = 0, 1, \ldots, N - 2$ and $l = 0, 1, \ldots, M - 2$. Matrix $\mathbf{B}$ is the transpose of the second derivative operator $\mathbf{A}$ and matrix $\mathbf{S}$ is a $(N - 1) \times (M - 1)$ matrix, which consists of the spectral coefficients of the source term for $k = 0, 1, \ldots, N - 2$ and $l = 0, 1, \ldots, M - 2$.

Following the Haidvogel-Zang procedure, operator $\mathbf{A}$ is diagonalized:

$$\mathbf{A} = \mathbf{Q}\mathbf{\Lambda}\mathbf{Q}^{-1}, \tag{3.24}$$

where $\mathbf{\Lambda}$ is a matrix with eigenvalues λ_k on the diagonal, and where the matrix $\mathbf{Q}$ contains columnwise the eigenvectors. Substitution of (3.24) in Eq. (3.23) and multiplying the result with $\mathbf{Q}^{-1}$ from the left, yields

$$\mathbf{\Lambda}\mathbf{C}^* + \mathbf{C}^*\mathbf{B} - \lambda \mathbf{C}^* = \mathbf{S}^*, \tag{3.25}$$

where $\mathbf{C}^*$ and $\mathbf{S}^*$ are the transformed matrices $\mathbf{Q}^{-1}\mathbf{C}$ and $\mathbf{Q}^{-1}\mathbf{S}$, respectively.

The diagonalization of $\mathbf{A}$ results in a set of $N - 1$ decoupled one dimensional Helmholtz equations

$$\hat{c}_{kl}^{*(02)} - (\lambda - \lambda_k)\hat{c}_{kl}^* = \hat{S}_{kl}^* \qquad\qquad \begin{array}{l} k = 0, 1, \ldots, N - 2, \\ l = 0, 1, \ldots, M - 2, \end{array} \tag{3.26}$$

with transformed boundary conditions

$$\hat{c}^*_{kM} = -\frac{1}{M^2} \sum_{\substack{l=0 \\ l \text{ even}}}^{M-2} l^2 \hat{c}^*_{kl} \qquad\qquad k = 0, 1, \dots, N-2, \qquad (3.27)$$

$$\hat{c}^*_{k,M-1} = -\frac{1}{(M-1)^2} \sum_{\substack{l=1 \\ l \text{ odd}}}^{M-3} l^2 \hat{c}^*_{kl} \qquad\qquad k = 0, 1, \dots, N-2. \qquad (3.28)$$

The one-dimensional equations are solved successively for $k = 0, 1, \dots, N-2$. After the solution matrix $\mathbf{C}^*$ has been transformed by multiplication with $\mathbf{Q}$ from the left, the highest modes $\hat{c}_{Nl}$ and $\hat{c}_{N-1,l}$ are obtained using Eqs. (3.12) and (3.13).

In order to keep Eq. (3.26) comprehensible, the asterix and the indices concerning the x direction are omitted. This results in

$$\hat{c}^{(2)}_l - \lambda' \hat{c}_l = \hat{S}_l \qquad\qquad l = 0, 1, \dots, M-2, \qquad (3.29)$$

where $\lambda' = (\lambda - \lambda_k)$. A very efficient solution procedure for Eq. (3.29) can be obtained using the recursion relation

$$2l\hat{c}^{(q-1)}_l = \bar{\bar{c}}_{l-1}\hat{c}^{(q)}_{l-1} - \hat{c}^{(q)}_{l+1}. \qquad (3.30)$$

This results in

$$\frac{\lambda' \bar{\bar{c}}_{l-2}}{4l(l-1)}\hat{c}_{l-2} + \left(1 - \frac{\lambda' \beta_l}{2l(l^2-1)}\right)\hat{c}_l + \frac{\lambda' \beta_{l+2}}{4l(l+1)}\hat{c}_{l+2} =$$
$$\frac{\bar{\bar{c}}_{l-2}}{4l(l-1)}\hat{S}_{l-2} - \frac{\beta_l}{2l(l^2-1)}\hat{S}_l + \frac{\beta_{l+2}}{4l(l+1)}\hat{S}_{l+2}, \qquad (3.31)$$

for $l = 2, 3, \dots, M$, where β_l is a constant

$$\beta_l = \begin{cases} 1 & 0 \le l \le M-2 \\ 0 & l > M-2 \end{cases}. \qquad (3.32)$$

Note that the even and odd coefficients are decoupled. The linear system for the even coefficients has a quasi-tridiagonal structure

$$\begin{pmatrix} 0 & 4 & 16 & \cdots & & & & M^2 \\ * & * & * & & & & & \\ & * & * & * & & & & \\ & & * & * & * & & & \\ & & & & \vdots & & & \\ & & & & * & * & * & \\ & & & & & * & * & \\ & & & & & & * & * \end{pmatrix} \begin{pmatrix} \hat{c}_0 \\ \hat{c}_2 \\ \hat{c}_4 \\ \hat{c}_6 \\ \vdots \\ \hat{c}_{M-4} \\ \hat{c}_{M-2} \\ \hat{c}_M \end{pmatrix} = \begin{pmatrix} 0 \\ \hat{f}_0 \\ \hat{f}_2 \\ \hat{f}_4 \\ \vdots \\ \hat{f}_{M-6} \\ \hat{f}_{M-4} \\ \hat{f}_{M-2} \end{pmatrix}, \qquad (3.33)$$

where the $*$'s denote the non-zero coefficients and $\hat{f}_l$ is the right-hand side of Eq. (3.31). The linear system for the odd coefficients has a similar structure; of course in this case the first row, which represents the boundary condition, contains $1, 9, 25, \dots, (M-1)^2$. Both systems can be solved efficiently using a modified Thomas algorithm.

3.1.3 Conservation of mass

The advection-diffusion equation with no-flux boundary condition satisfies conservation of mass, i.e.,

$$\frac{d}{dt} \iint_{\mathcal{D}} c \, dA = 0. \tag{3.34}$$

Naturally, it is desirable for the discrete solution to satisfy this conservation law as well. The discrete analogue of the integration over the whole domain is given by a summation of the Chebyshev coefficients:

$$\iint_{\mathcal{D}} c \, dA = 4 \sum_{\substack{k=0 \\ k \text{ even}}}^{N} \sum_{\substack{l=0 \\ l \text{ even}}}^{M} \frac{\hat{c}_{kl}}{(k^2 - 1)(l^2 - 1)}. \tag{3.35}$$

Consider the conservation of mass at one time-integration step. In order to explain the conservation properties, we have divided the solution procedure at a time level into two steps. The first step consists of the computation of the source S by evaluating the explicit terms. The integration of Eq. (3.5) results in[2]

$$\sum_{\substack{k=0 \\ k \text{ even}}}^{N} \sum_{\substack{l=0 \\ l \text{ even}}}^{M} \frac{\hat{S}_{kl}^{n,n-1}}{(k^2 - 1)(l^2 - 1)} =$$

$$- \sum_{\substack{k=0 \\ k \text{ even}}}^{N} \sum_{\substack{l=0 \\ l \text{ even}}}^{M} \frac{\nabla^2 \hat{c}_{kl}^n}{(k^2 - 1)(l^2 - 1)} - \lambda \sum_{\substack{k=0 \\ k \text{ even}}}^{N} \sum_{\substack{l=0 \\ l \text{ even}}}^{M} \frac{\hat{c}_{kl}^n}{(k^2 - 1)(l^2 - 1)} +$$

$$\text{Pe} \sum_{\substack{k=0 \\ k \text{ even}}}^{N} \sum_{\substack{l=0 \\ l \text{ even}}}^{M} \frac{\hat{\mathcal{L}}_{kl}^{n,n-1}}{(k^2 - 1)(l^2 - 1)}, \tag{3.36}$$

where $\hat{\mathcal{L}}_{kl}$ are the Chebyshev coefficients of the part between square brackets in Eq. (3.5). The Chebyshev coefficients of the linear terms can be calculated exactly and therefore, the integral conditions concerning these terms are satisfied exactly. The nonlinear terms are computed pseudospectrally using the padding technique to avoid aliasing. In this technique extra modes are added to the double series of Chebyshev polynomials. These extended series, where the coefficients of the extra modes are zero, are transformed to physical space. After multiplication in physical space the result is transformed back to spectral space using all modes. Then, the series are truncated for further calculations by dropping the extra modes (which are not zero anymore). Although the remaining $(N + 1)(M + 1)$ modes are exact, they cannot represent all $(2N + 1)(2M + 1)$ modes from the convolution sum. After all, the complete approximation of quadratic nonlinearities consists of $2N + 1$ modes:

$$u(x)v(x) = \left(\sum_{k=0}^{N} \hat{u}_k T_k(x) \right) \left(\sum_{l=0}^{N} \hat{v}_l T_l(x) \right) = \sum_{k=0}^{2N} \widehat{uv}_k T_k(x). \tag{3.37}$$

---

[2]The subscript of λ_c and S_c is omitted.

Due to this truncation the integral condition $\iint(\mathbf{u} \cdot \nabla)c \; dA = 0$ is not exactly satisfied anymore. However, the truncation error is related to the highest modes and decays faster than algebraically in $1/N$ (this property is termed spectral accuracy).

The second step of the solution procedure at every time level consists of the solution of the Helmholtz equation. Integration of Eq. (3.3) yields

$$\sum_{\substack{k=0 \\ k \text{ even } l \text{ even}}}^{N} \sum_{l=0}^{M} \frac{\nabla^2 \hat{c}_{kl}^{n+1}}{(k^2 - 1)(l^2 - 1)} - \lambda \sum_{\substack{k=0 \\ k \text{ even } l \text{ even}}}^{N} \sum_{l=0}^{M} \frac{\hat{c}_{kl}^{n+1}}{(k^2 - 1)(l^2 - 1)} =$$

$$\sum_{\substack{k=0 \\ k \text{ even } l \text{ even}}}^{N} \sum_{l=0}^{M} \frac{\hat{S}_{kl}^{n,n-1}}{(k^2 - 1)(l^2 - 1)}. \qquad (3.38)$$

Since the first term of the left-hand side equals zero, Eq. (3.38) together with (3.36) would in the ideal case represent conservation of mass:

$$\sum_{\substack{k=0 \\ k \text{ even } l \text{ even}}}^{N} \sum_{l=0}^{M} \frac{\hat{c}_{kl}^{n+1} - \hat{c}_{kl}^{n}}{(k^2 - 1)(l^2 - 1)} = 0. \qquad (3.39)$$

However, as can be seen in Section 3.1.2, the solution procedure of the Helmholtz equation does not involve the high frequency modes of $S^{n,n-1}$. In other words, the discrete equation that is actually solved can be expressed as

$$(\nabla^2 - \lambda)c^{n+1} = S^{n,n-1} + B^{n+1}, \qquad (3.40)$$

where B again represents high frequency modes, which are not known *a priori*. Integration of Eq. (3.40) results in

$$\sum_{\substack{k=0 \\ k \text{ even } l \text{ even}}}^{N} \sum_{l=0}^{M} \frac{S_{kl}^{n,n-1} + \lambda \hat{c}_{kl}^{n+1}}{(k^2 - 1)(l^2 - 1)} = -\sum_{\substack{k=0 \\ k \text{ even } l \text{ even}}}^{N} \sum_{l=0}^{M} \frac{\hat{B}_{kl}^{n+1}}{(k^2 - 1)(l^2 - 1)}. \qquad (3.41)$$

Generally, the right-hand side of (3.41) is not zero, causing an error in the conservation of mass. Again the error is related to the high-frequency modes and therefore it decays exponentially in N.

Note that, in contrast to the conservation of total concentration, the integral condition concerning the Navier-Stokes equations is satisfied within machine accuracy:

$$\iint_{\mathcal{D}} \omega \; dA = \oint_{\partial \mathcal{D}} \mathbf{u} \; d\ell. \qquad (3.42)$$

However, this condition is not related to time integration, but it is obtained by application of Stokes' theorem using $\omega = \nabla \times \mathbf{u}$. Since the definition of the vorticity is enforced by the influence matrix method, Equation (3.42) is satisfied exactly.

3.2 Lagrangian Approach

Mixing in flows has been investigated using the Lagrangian approach in many branches of fluid dynamics. Examples are the very efficient mixing by two agitators running alternatingly [1], the mixing properties of geophysical flows [2], chaotic advection and anomalous diffusion in Rayleigh-Bénard convection [3], and many others, including industrial flow problems. The chaotic transport properties of these flows are studied by following a large number of passive tracers.

3.2.1 Time scheme

The position of a particle, $\mathbf{x}(t)$, is given by the Lagrangian description of motion. The particle trajectory is related to the velocity field by:

$$\frac{d\mathbf{x}}{dt} = \mathbf{u}(\mathbf{x}, t), \tag{3.43}$$

with initial condition $\mathbf{x}(0) = \mathbf{x}_0$.

The integration of Eq. (3.43) is carried out simultaneously with the Navier-Stokes simulation, which provides the velocity at integer time steps. We use a fourth-order predictor-corrector technique that consists of a fourth-order Adams-Bashforth predictor:[3]

$$\mathbf{x}_p = \mathbf{x}^n + \frac{\Delta t}{24} \left[55\mathbf{u}^n - 59\mathbf{u}^{n-1} + 37\mathbf{u}^{n-2} - 9\mathbf{u}^{n-3} \right], \tag{3.44}$$

and a fourth-order Adams-Moulton corrector:

$$\mathbf{x}^{n+1} = \mathbf{x}_p + \frac{\Delta t}{24} \left[9\mathbf{u}_p + 19\mathbf{u}^n - 5\mathbf{u}^{n-1} + \mathbf{u}^{n-2} \right]. \tag{3.45}$$

Because this predictor-corrector method is not self-starting, we have to use an alternative procedure for the initial time steps. The first time integration step is calculated using a fourth-order Runge-Kutta method. The next step consists of a third-order predictor and a fourth-order corrector:

$$\mathbf{x}_p = \mathbf{x}^1 + \frac{\Delta t}{6} \left[19\mathbf{u}^1 - 20\mathbf{u}^{1/2} + 7\mathbf{u}^0 \right], \tag{3.46}$$

$$\mathbf{x}^2 = \mathbf{x}_p + \frac{\Delta t}{6} \left[2\mathbf{u}_p + 7\mathbf{u}^1 - 4\mathbf{u}^{1/2} + \mathbf{u}^0 \right]. \tag{3.47}$$

These first two steps both evaluate the velocity at $t = 1/2$, which follows from the Runge-Kutta integration of the first time step of the Navier-Stokes equation. The third time step consist of the same predictor-corrector combination, but now based on other time levels:

$$\mathbf{x}_p = \mathbf{x}^2 + \frac{\Delta t}{12} \left[23\mathbf{u}^2 - 16\mathbf{u}^1 + 5\mathbf{u}^0 \right], \tag{3.48}$$

$$\mathbf{x}^3 = \mathbf{x}_p + \frac{\Delta t}{24} \left[9\mathbf{u}_p + 19\mathbf{u}^2 - 5\mathbf{u}^1 + \mathbf{u}^0 \right]. \tag{3.49}$$

The combination of these schemes is tested and found to be fourth-order accurate.

---

[3]The superscripts denote the time level.

An alternative for this predictor-corrector technique can be found in the Runge-Kutta method. A classical fourth-order Runge-Kutta scheme can be implemented if the intermediate solution needed for this method is evaluated at the odd time levels. This enlarges the effective time step to $2\Delta t$, which reduces the accuracy of the time scheme. However, the advantage of a Runge-Kutta method is the possibility to add extra tracers at any time step. For techniques like interface tracking as described by Xue & Tangborn [16], this is needed to prevent loss of detail of the interface.

Since the particles are not generally at a grid point, we need to calculate the velocity of the tracer by a direct transformation from spectral to physical space. This is achieved by evaluating Eq. (2.10) at the position of the particle. In consequence of this, the determination of the velocity of N_p particles has an operation count of $\mathcal{O}(N_p N M)$.

3.2.2 Diffusion

The Lagrangian method described so far does not include diffusion. Simulation of diffusion can be accomplished by a random-walk method which uses a Lagrangian approach based on the stochastic differential corresponding to the scalar advection-diffusion equation. Saffman [17] used a random-walk approach to study the effects of molecular diffusion on the transport of a passive scalar in flow through porous media. For a brief survey with view to applications in numerical schemes based on random-walk methods, see Chorin & Marsden [18].

In the random-walk method a particle in the flow is advanced according to

$$\mathbf{x}^{n+1} = \mathbf{x}^n + \Delta \mathbf{x}^n + \boldsymbol{\eta}, \tag{3.50}$$

where $\Delta \mathbf{x}^n$ is the deterministic jump in a time step Δt, calculated using the method described before, and where $\boldsymbol{\eta}$ is a random component describing the Brownian motion of the molecules. The components of $\boldsymbol{\eta}$ are Gaussianly distributed random variables, each with zero mean and variance $2\Delta t/\mathrm{Pe}$, which are generated using standard algorithms based on the Box-Müller transformation (e.g., see Press *et al.* [19]).

Error-estimation techniques show the accuracy of the random-walk method to be $\mathcal{O}(N_p^{-1/2})$. The slow convergence, which is typical of random-walk methods, requires that N_p be very large for accurate solutions. In our computations the number of particles is limited by computational resources to $\mathcal{O}(10^4)$ resulting in an error of a few percent.

A subtle point which needs our attention is the combination of the time scheme and a random-walk method. The predictor-corrector technique used in our simulations is based on an extrapolation of the velocity using previous time levels. The superposition of a random component disturbs this extrapolation technique: the velocities at the previous time levels contain an "error" $\Delta \mathbf{u}$ of magnitude $\mathcal{O}(|\boldsymbol{\eta}| \left| \frac{\partial \mathbf{u}}{\partial \mathbf{x}} \right|)$. This error results in an extra displacement, which can be added to Eq. (3.50)

$$\mathbf{x}^{n+1} = \mathbf{x}^n + \Delta \mathbf{x}^n + \boldsymbol{\eta} + \mathcal{O}(\Delta t \Delta \mathbf{u}). \tag{3.51}$$

It can be seen that for a small time step this error is actually much smaller than the random component and therefore, it can be neglected. Moreover, simulation of the diffusion of a point in a fluid in solid

body rotation, showed that the accuracy of this method is not affected by the error arising from this interference. Note that Runge-Kutta schemes do not suffer from this disturbance, since they do not use previous time levels.

3.3 Characterization of Mixing

3.3.1 Anomalous diffusion

Transport in a fluid flow can be characterized by the variance of a tracer cloud about its mean position denoted by σ^2, which for normal diffusive processes grow linearly with time: $\sigma^2 \sim t^\alpha$ with $\alpha = 1$. Processes with $\alpha \neq 1$ are termed anomalous diffusion.

Hypodiffusion ($\alpha < 1$) can take place when "traps" embedded in the flow, inhibit the motion of the tracer. Trapping can occur in two-dimensional cellular flows. For instance, Guyon *et al.* [20] argue that in a spatially periodic two-dimensional series of convection rolls between slippery boundaries, $\alpha = 1/2$. If the rolls are enclosed by rigid boundaries, $\alpha = 2/3$ (Young, Pumir & Pomeau [21]). The latter result was confirmed by the experiments of Cardoso & Tabeling in Rayleigh-Bénard convection [22]. Experiments of dispersion in a quasi-two-dimensional periodic flow revealed $\alpha = 2/3$ as well [23].

Superdiffusion ($\alpha > 1$) can occur if tracer trajectories in the flow have long excursions. These excursions are termed Lévy flights, which are well known mathematically, and are recently observed by Solomon, Weeks & Swinney in a 2D flow in a rotating annulus [24].

Determination of the variance is very straightforward. In case of the Lagrangian approach the variance can be computed by summation over all particles:

$$\sigma^2 = \frac{1}{N_p} \sum_{i=1}^{N_p} |\mathbf{x}_i - \bar{\mathbf{x}}|^2, \tag{3.52}$$

where $\bar{\mathbf{x}}$ is the mean position defined as $\frac{1}{N_p} \sum_{i=1}^{N_p} \mathbf{x}_i$. In the Eulerian approach this results in the continuous form of (3.52):

$$\sigma^2 = \frac{\iint |\mathbf{x} - \bar{\mathbf{x}}|^2 c(\mathbf{x}) \, dA}{\iint c(\mathbf{x}) \, dA}, \tag{3.53}$$

with

$$\bar{\mathbf{x}} = \frac{\iint \mathbf{x} c(\mathbf{x}) \, dA}{\iint c(\mathbf{x}) \, dA}. \tag{3.54}$$

These equations can be recast in a summation over the Chebyshev expansion coefficients. Note that the initial value of the variance is not zero but depends on the spread of the initial tracer distribution.

3.3.2 Correlation dimension

The variance of a tracer cloud about its mean position gives us useful information about dispersion processes. However, for characterizing the degree of mixedness, the measurement of σ is often insuf-

ficient. The variance already attains nearly its maximum value for a single filament snaking through the flow, at a stage when the tracer is not at all well mixed.

Another approach, which has been developed recently, uses the correlation integral $C(\ell)$ to characterize mixing. The correlation integral is defined as

$$C(\ell) = \int\limits_0^\ell d\mathbf{r}\, \xi(\mathbf{r}),$$ (3.55)

where ξ is the standard correlation function

$$\xi(\mathbf{r}) = \int d\mathbf{x}\, c(\mathbf{x} - \mathbf{r})c(\mathbf{x}).$$ (3.56)

A definition of the correlation integral in words is the number of tracer pairs whose distance is less than ℓ. When $C(\ell)$ exhibits a subrange in which

$$C(\ell) \sim \ell^\mu,$$ (3.57)

then μ is the correlation exponent, characterizing the geometry at the corresponding length scales. Some particular values of μ are the following: $\mu = 0$ corresponds to tracers clustered at a point, $\mu = 1$ corresponds to well-separated filaments of tracer, and $\mu = 2$ corresponds to an area-filling cloud; the whole panoply of intermediate structures associated with fractional μ is also available.

Summarizing, the slope of the correlation integral in a log-log plot reveals the degree of mixedness: a steep slope means well-mixed. In order to estimate mixing times the correlation integral should be considered at several times. How the correlation integral is used to characterize the degree of mixedness is illustrated in Section 4.2.2.

Grassberger & Procaccia [25] argue that μ is closely related to the information dimension and the fractal dimension, which is often determined by box-counting techniques. The relation between the fractal dimension of the iso-concentration lines and the velocity field, is given by several exact inequalities concerning μ and structure function exponents of the velocity and concentration fields [26]. Experiments performed in a 2D turbulent flow [23] seem to be consistent with them.

In the Lagrangian approach the correlation function is computed in the following manner. First, compute the $N_p(N_p - 1)/2$ distances between all pairs of particles, then $C(\ell)$ is defined as the number of pairs with distance less than ℓ. For the continuous approach the determination of $C(\ell)$ is not straightforward and is very time-consuming; $\mathcal{O}(N^2 M^2)$ operations are needed for each given ℓ. Nevertheless, machine accuracy is reached.

Chapter 4

Simulations

In this chapter we present the results of the numerical simulations. We describe the results of three different problems:

- **Natural convection in a square cavity** This is a popular problem for comparing algorithms designed to solve the Navier-Stokes equations in the Boussinesq approximation. It is also a test for the implementation of the numerical algorithm developed to solve the advection-diffusion equation for a tracer.

- **Spin-up in a square container** This problem is used to estimate the accuracy of the numerical algorithms based on both the Eulerian and Lagrangian approach.

- **Linear array of vortices** In order to show an application of the developed methods we have simulated the dispersion of a passive tracer in a periodic cellular flow.

4.1 Natural Convection in a Square Cavity

The thermally driven square cavity with adiabatic top and bottom walls is one of the classical problems in the heat transfer literature. Moreover, it has become one of the most popular test-problems to compare numerical algorithms designed for the integration of the Navier-Stokes equations of incompressible recirculating flows. Note that this problem is free of any singularity in the boundary conditions except the presence of the corners. This makes it more attractive than other problems, such as the driven cavity configuration, for example, to test the accuracy of high precision schemes. Another advantage of the thermally driven cavity is the fact that it can be used for testing the implementation of the algorithm based on the Eulerian approach, since the temperature of the fluid can be considered as a tracer.

Consider the flow of a Newtonian fluid of kinematic viscosity ν, thermal diffusivity κ and thermal expansion coefficient β enclosed in a square cavity of height L. The coordinate system is defined so that the y-axis points vertically upwards in the direction opposite to the gravity vector of modulus g. The

x-axis is horizontal. Constant uniform temperatures θ_h and θ_c ($\Delta\theta = \theta_h - \theta_c > 0$) are imposed at the left and right vertical walls, respectively. The top and bottom horizontal walls are considered perfectly adiabatic. The resulting flow is assumed to be two-dimensional and the temperature difference is small enough so that the Boussinesq approximation holds.

The governing equations are cast in dimensionless form using scaling variables as proposed by Le Quéré [27]. Using the scaling factors $\Delta\theta$ for temperature, L for length, $(\kappa/L)\mathrm{Ra}^{1/2}$ for velocity, where $\mathrm{Ra} = (g\beta\Delta\theta L^3)/\nu\kappa$ is the Rayleigh number, and the relating scaling factor for time $(L^2/\kappa)\mathrm{Ra}^{-1/2}$, the governing equations read

$$\frac{\partial\omega}{\partial t} + (\mathbf{u}\cdot\nabla)\omega = \frac{\mathrm{Pr}}{\mathrm{Ra}^{1/2}}\nabla^2\omega + \mathrm{Pr}\frac{\partial\theta}{\partial x} \tag{4.1}$$

$$\frac{\partial\theta}{\partial t} + (\mathbf{u}\cdot\nabla)\theta = \frac{1}{\mathrm{Ra}^{1/2}}\nabla^2\theta \tag{4.2}$$

$$\nabla\cdot\mathbf{u} = 0. \tag{4.3}$$

The value of the Prandtl number was set to 0.71, which corresponds to a cavity filled with air. In order to coincide with the literature we have transformed our computational domain in such a way that the dimensionless domain extends from 0 to 1 in both the x and y directions. The boundary conditions for the temperature are then:

$$\theta = 1 \qquad\qquad \text{at } x = 0 \tag{4.4}$$

$$\theta = 0 \qquad\qquad \text{at } x = 1 \tag{4.5}$$

$$\frac{\partial\theta}{\partial y} = 0 \qquad\qquad \text{at } y = 0 \text{ and } y = 1. \tag{4.6}$$

The solution of the 2D Boussinesq equations in this configuration becomes unsteady for a value of Ra very close to 2×10^8. For the Rayleigh numbers 10^3, 10^4, 10^5 and 10^6 De Vahl Davis [28] provided "benchmark solutions" that were obtained with a second-order finite difference scheme and a Richardson extrapolation scheme. Accurate solutions at $\mathrm{Ra} = 10^6$, 10^7 and 10^8 have been obtained by Le Quéré [27] using a pseudospectral Chebyshev algorithm.

The steady-state solution corresponding to the Ra value of 10^8 is presented in Figure 4.1 by means of temperature and stream function contours. The following characteristic values of the steady-state solutions are determined:

$|\psi|_{\mathrm{mid}}$ the absolute value of the stream function at the mid-point of the cavity,

$|\psi|_{\mathrm{max}}$ the maximum of the absolute value of the stream function together with its location,

u_{max} the maximum horizontal velocity on the vertical mid-plane of the cavity together with its location,

v_{max} the maximum vertical velocity on the horizontal mid-plane of the cavity together with its location,

Nu   the average Nusselt number on the left boundary (this is equivalent to the rate of heat transfer across the cavity),
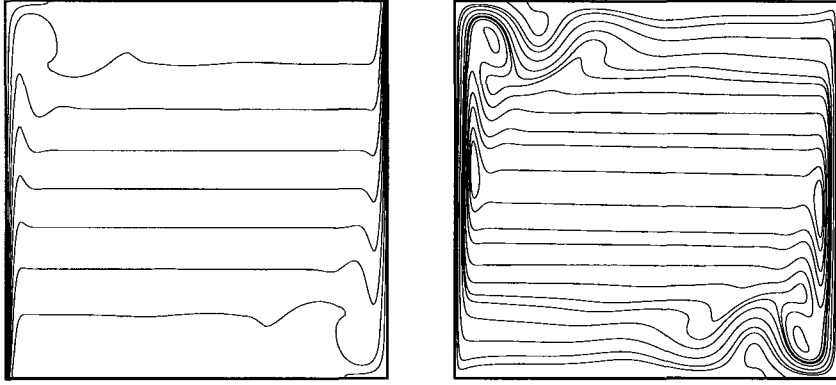
Figure 4.1: $Ra = 10^8$. Isotherms (left) and stream function (right).

Nu_{max} the maximum value of the local Nusselt number on the left boundary together with its location,

Nu_{min} the minimum value of the local Nusselt number on the left boundary together with its location.

The local Nusselt number is defined as the heat flux in horizontal direction:

$$Nu = Ra^{1/2} u + \frac{\partial \theta}{\partial x}. \qquad (4.7)$$

In Tables 4.1 and 4.2 the values are listed together with the benchmark solutions. The solutions at $Ra = 10^3$, 10^4 and 10^5 are consistent with the results from De Vahl Davis, considering the estimated error of 0.1% in the benchmark values. At higher Rayleigh numbers the similarity between the present results and the solution obtained by Le Quéré is exact. Note that there seems to be a discrepancy in the last digit for some values. However, this is caused by round-off errors.

Ra	10^3		10^4		10^5	
	Present	Ref. [28]	Present	Ref. [28]	Present	Ref. [28]
$|\psi|_{\text{mid}} \times 10^2$	3.715	3.713	5.074	5.074	2.883	2.883
$|\psi|_{\text{max}} \times 10^2$	—	—	—	—	3.041	3.040
x	—	—	—	—	0.285	0.285
y	—	—	—	—	0.601	0.601
$u_{\text{max}} \times 10$	1.154	1.154	1.618	1.618	1.099	1.098
y	0.814	0.813	0.823	0.823	0.855	0.855
$v_{\text{max}} \times 10$	1.169	1.169	1.963	1.962	2.170	2.169
x	0.178	0.178	0.119	0.119	0.066	0.066
Nu	1.118	1.118	2.245	2.243	4.522	4.519
Nu_{max}	1.506	1.505	3.531	3.528	7.720	7.717
y	0.089	0.092	0.144	0.143	0.082	0.081
Nu_{min}	0.691	0.692	0.585	0.586	0.728	0.729
y	1.000	1.000	1.000	1.000	1.000	1.000

Table 4.1: Characteristics of the steady-state solution for Rayleigh numbers 10^3, 10^4 and 10^5 in comparison with the benchmark solution from De Vahl Davis [28].

Ra	10^6		10^7		10^8	
	Present	Ref. [27]	Present	Ref. [27]	Present	Ref. [27]
$|\psi|_{\text{mid}} \times 10^3$	16.386	16.386	9.2849	9.285	5.2322	5.232
$|\psi|_{\text{max}} \times 10^3$	16.811	16.811	9.5387	9.539	5.3848	5.385
x	0.1504	0.150	0.0860	0.086	0.0483	0.048
y	0.5467	0.547	0.5556	0.556	0.5525	0.553
$u_{\text{max}} \times 10^2$	6.4834	6.483	4.6987	4.699	3.2188	3.219
y	0.8499	0.850	0.8793	0.879	0.9279	0.928
$v_{\text{max}} \times 10$	2.2056	2.206	2.2115	2.211	2.2224	2.222
x	0.0381	0.038	0.0213	0.021	0.0121	0.012
Nu	8.8252	8.825	16.523	16.523	30.255	30.255
Nu_{max}	17.536	17.536	39.395	39.39	87.245	87.24
y	0.0392	0.039	0.0180	0.018	0.0083	0.008
Nu_{min}	0.9795	0.9795	1.3663	1.366	1.9191	1.919
y	1.0000	1.000	1.0000	1.000	1.0000	1.000

Table 4.2: Characteristics of the steady-state solution for Rayleigh numbers 10^6, 10^7 and 10^8 in comparison with the benchmark solution from Le Quéré [27].

4.2 Spin-up in a Square Container

Spin-up is the adjustment process of fluid in a container, initially rotating with angular velocity Ω, after a sudden change of the rotational velocity of the container from Ω to $\Omega + \Delta\Omega$ at $t = 0$. Experimental studies on spin-up of fluid in rectangular and square containers were recently reported by Van Heijst, Davies and Davis [29] and Van de Konijnenberg [30]. An important feature of rotating flows is the existence of a two-dimensionalization mechanism which enables one to study specific aspects of rotating flows by 2D numerical simulations. To lowest order the flow dynamics in spin-up experiments in square or rectangular containers is a two-dimensional phenomenon, as well. Numerical simulations of 2D spin-up in rectangular containers have been reported by Suh [31], Vissers [32], Tacken [33] and Willemen [10].

In a coordinate system corotating with the container one observes a large anticyclonic[1] cell that fills the domain entirely; this motion arises because of the inability of the fluid to follow the change in rotation of the boundaries. At $t = 0^+$ boundary layers are formed and cyclonic vorticity, generated in the boundary layers, is advected by the primary anticyclonic flow along the sides of the container. In the subsequent stage it is observed that, when the Reynolds number is large enough, boundary layer separation takes place and the advected cyclonic vorticity gets accumulated in small cyclonic cells in the corners of the container. In case of a square container these corner vortices are of equal strength because of symmetry reasons.[2] For low Reynolds numbers a quasi-steady state sets in, since the decay of the cells occurs on a time scale considerably larger than the eddy turnover time scale, which is of the order $2\pi/\Delta\Omega$. For higher Reynolds numbers, the vorticity generated in the boundary layers will perturb the core vortex, hence affecting the transport properties of the flow.

Consider 2D spin-up in a square container, with sidewalls of length L. The starting flow can be obtained by solving the Poisson equation for the stream function at $t = 0$, $\nabla^2\psi = 2\Delta\Omega$ with $\psi = 0$ at the boundaries of the domain [30]. The components of the velocity can be derived via the definition of the stream function: $u = \frac{\partial\psi}{\partial y}$ and $v = -\frac{\partial\psi}{\partial x}$. The boundary condition for the normal component of the velocity is satisfied, but the tangential velocity of the starting flow is not zero at the boundary. In order to satisfy the no-slip condition an extremely thin boundary layer is set up at $t = 0^+$. An alternative initial condition is found by simply assuming solid-body rotation of the fluid with respect to the corotating coordinate system. The starting flow is given by $\mathbf{u} = \Delta\Omega(\mathbf{r} \times \mathbf{k})$, and violates the boundary conditions for both the normal and tangential components of the velocity. However, this starting flow satisfies conservation of mass. The boundary conditions are corrected in the first integration step and both initial flows give the same numerical results [4].

In dimensionless coordinates the computational domain extends from -1 to 1 in both the x and y directions. We have simulated spin-up for several values of the Reynolds number, which is here defined as $\mathrm{Re} = \frac{L^2\Delta\Omega}{4\nu}$.

Note that the investigation of mixing during spin-up is beyond the scope of this report. We have

---

[1]Anticyclonic vortices rotate faster than the container, whereas cyclonic vortices rotate slower than the container.

[2]For very high Reynolds numbers the symmetry in the flow pattern can be broken by turbulence.

only used this particular flow to test the numerical schemes based on both the Eulerian and Lagrangian approach for simulating the advection of passive tracers.

4.2.1 Eulerian approach

Simulations of spin-up have been performed for two different values of the Reynolds number: Re = 1000 and Re = 2500. Due to the appearance of very thin boundary layers at $t = 0^{+}$, in which the vorticity can have large values, simulations at these Reynolds numbers are quite difficult to perform. In order to avoid disturbance of oscillations arising from the singular character of the initial conditions, the initial stage of the spin-up is simulated without any tracer. At $t = 2$ the vorticity profiles have converged and corner vortices have been formed.[3] At this time a Gaussian blob of tracer, with an e-folding value of 0.1, is placed in the upper right corner and t is reset to zero. This initial tracer distribution is multiplied with the function $f(x, y) = (1 - e^{-20(1-x^2)^2})(1 - e^{-20(1-y^2)^2})$ in order to satisfy the homogeneous Neumann boundary conditions.

The process of mixing during spin-up with Re = 2500 and Pe = 5000, is illustrated in Figure 4.2 by means of snapshots of the tracer distribution at several times. Part of the blob, initially placed in the upper right corner ($t = 0$), is advected by the primary anticyclonic cell ($t = 4$ and $t = 8$). At $t = 8$ the corner cell starts to move along the boundary, hereby transporting the tracer in its core. However, this cell is squeezed between the primary cell and the right wall, and does not survive. The tracer is advected further along the edge of the anticyclonic cell and is mixed throughout the region outside the primary cell ($t = 12, 16, 20$).

Figures 4.3 and 4.4 show the variance σ^2 (defined by Eq. (3.53)) for several values of the Reynolds and Peclet number as a function of time. In all simulations the variance increases substantially during the first half rotation period ($t \leq \pi$). This is caused by the filament of tracer which is advected from the blob to the lower left corner of the container. When the head of the filament returns in the direction of the blob (see Figure 4.2), the variance decreases. At later times the variance seems to have reached a quasi-constant value of $\sigma^2 \approx 1$.

In order to estimate the accuracy of the values of σ^2, we have compared the results of calculations which have been performed with different numbers of Chebyshev polynomials N.[4] The time-integration step was the same for both simulations, i.e., $\Delta t = 5 \times 10^{-4}$. Figure 4.5 shows the difference ϵ_σ in σ^2 between computations of spin-up at Re = 1000 with $N = 120$ and $N = 104$. Starting at 10^{-10} the difference increases a few orders of magnitude during the first half rotation period. Hereafter ϵ_σ seems to stabilize around 10^{-7} and 10^{-5} for calculations with Pe = 1000 and Pe = 5000, respectively. In case Re = 2500 a similar evolution takes place, but the resulting difference is one order of magnitude larger for the simulations at both Pe = 1000 and Pe = 5000.

A reason for this discrepancy can be found in the accuracy of the velocity field. Since the velocity

---

[3]One rotation period of the container with respect to the original angular velocity of the container at $t < 0$ corresponds with a dimensionless time $t = 2\pi$.

[4]Actually the number of Chebyshev polynomials is $N + 1$, since the index runs from 0 to N. However, for the sake of simplicity we refer to N as the number of Chebyshev polynomials used for the computations. Also note that $M = N$ for all simulations on a square domain.
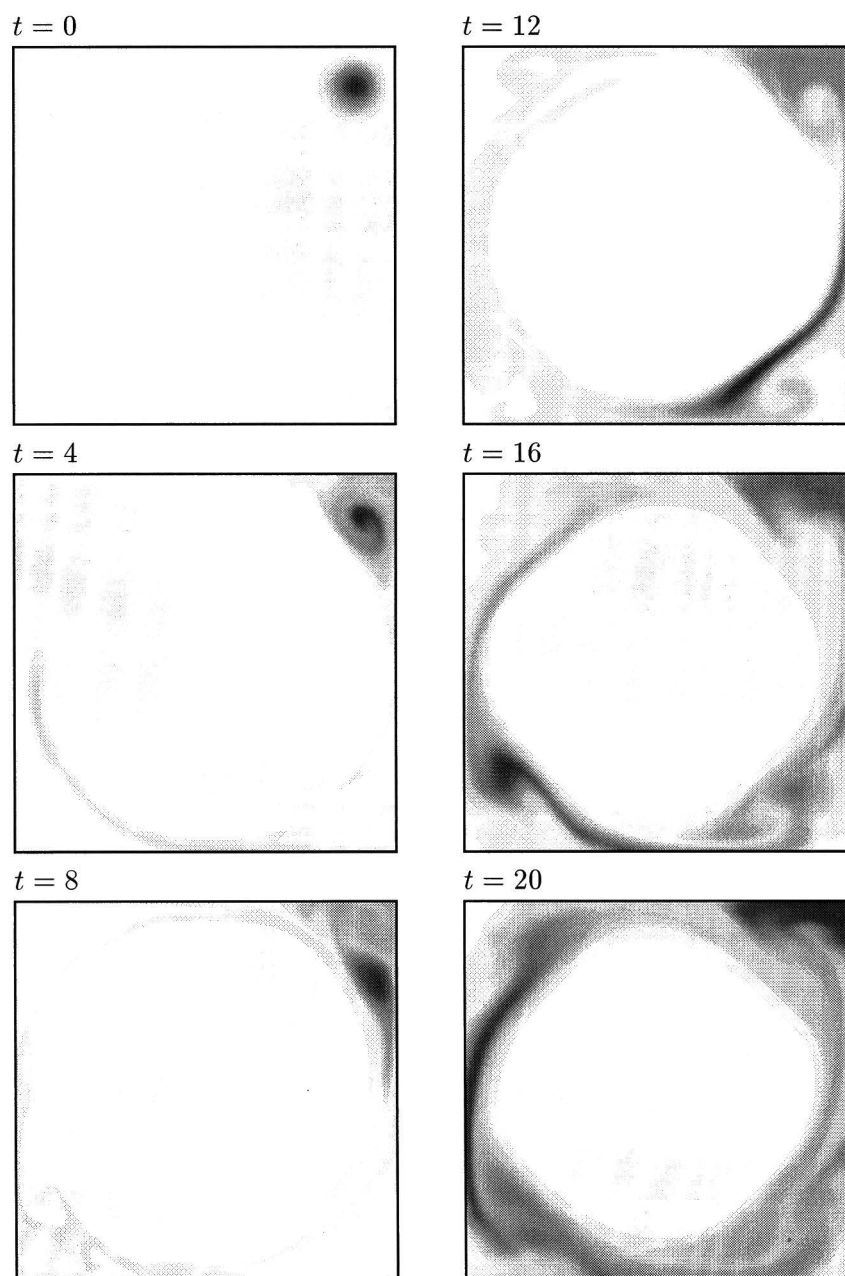
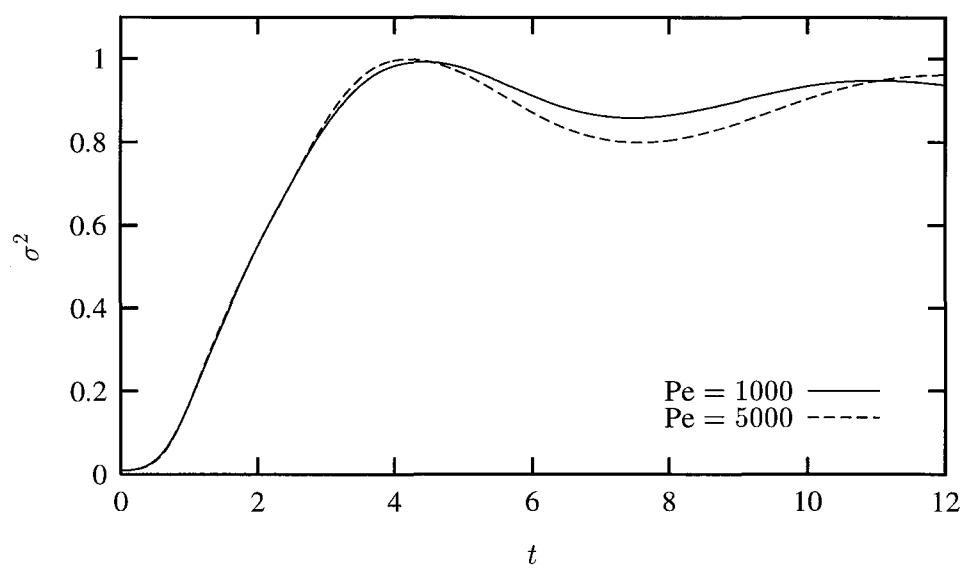**Figure 4.2:** Mixing of a passive tracer during spin-up: Re = 2500 and Pe = 5000.

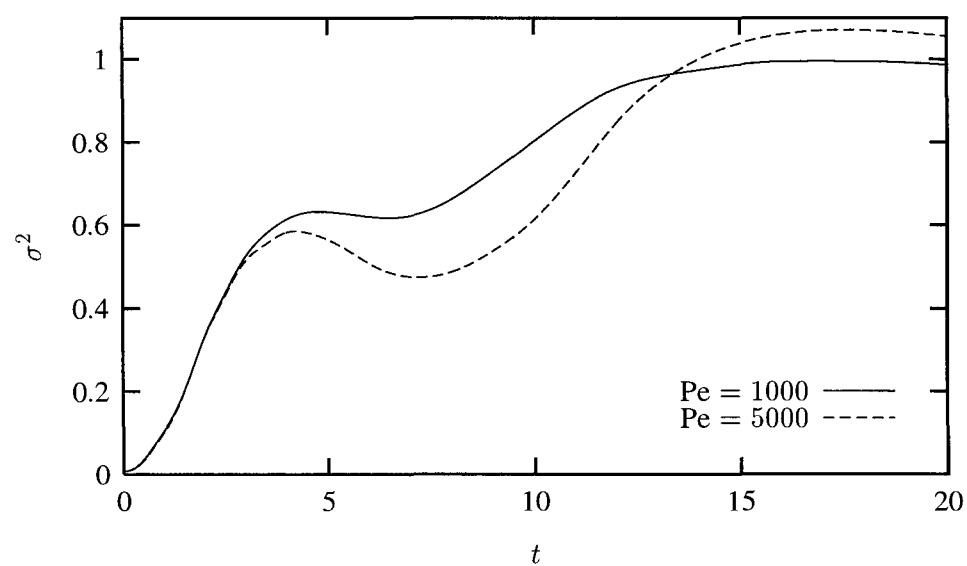**Figure 4.3:** The variance of the tracer cloud during spin-up, Re = 1000.

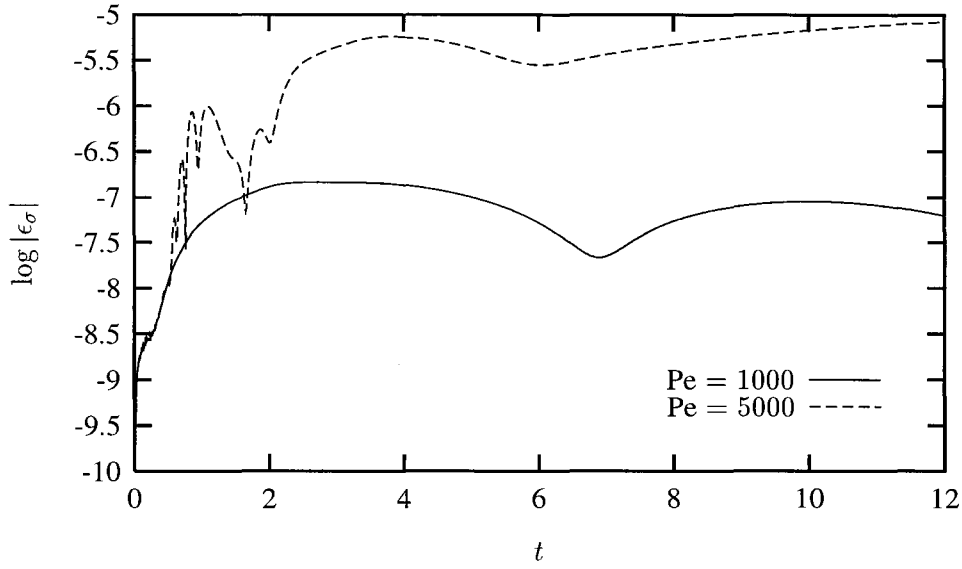**Figure 4.4:** The variance of the tracer cloud during spin-up, Re = 2500.

Figure 4.5: Absolute difference ϵ_σ in σ^2 between calculations performed with 104 and 120 Chebyshev modes for Re = 1000.

is an input for the advection-diffusion equation, we cannot expect the tracer field to be more accurate. If we compare the velocity fields at $t = 0$ calculated with $N = 104$ and $N = 120$, we find an average difference of order 10^{-8} in case Re = 2500. In the corners and along the sides of the container local differences of order 10^{-5} occur. For Re = 1000 these differences are somewhat smaller: 10^{-10} and 10^{-7}, respectively.

Another indication of the accuracy of the numerical method is the ability of the algorithm to satisfy the conservation of mass. In Section 3.1.3 we have demonstrated that the conservation of mass is not exact in the discrete solution. Here we define two errors which correspond to the two steps as presented in Section 3.1.3. The first error corresponds to the calculation of the source $S^{n,n-1}$ using previous time levels:

$$\epsilon_{\mathrm{I}} = \sum_{\substack{k=0 \\ k \text{ even}}}^{N} \sum_{\substack{l=0 \\ l \text{ even}}}^{M} \frac{\hat{c}_{kl}^{n} + \frac{1}{\lambda}\hat{S}_{kl}^{n,n-1}}{(k^2 - 1)(l^2 - 1)}. \tag{4.8}$$

The solution procedure of the Helmholtz equation causes the second error

$$\epsilon_{\mathrm{II}} = \sum_{\substack{k=0 \\ k \text{ even}}}^{N} \sum_{\substack{l=0 \\ l \text{ even}}}^{M} \frac{\hat{c}_{kl}^{n+1} + \frac{1}{\lambda}\hat{S}_{kl}^{n,n-1}}{(k^2 - 1)(l^2 - 1)}. \tag{4.9}$$

Figure 4.6 shows the errors ϵ_{I} and ϵ_{II} as a function of time.[5] The time-evolution of both errors is approximately the same, because they are both related to the high frequency modes. Subtraction of Eq. (4.8)

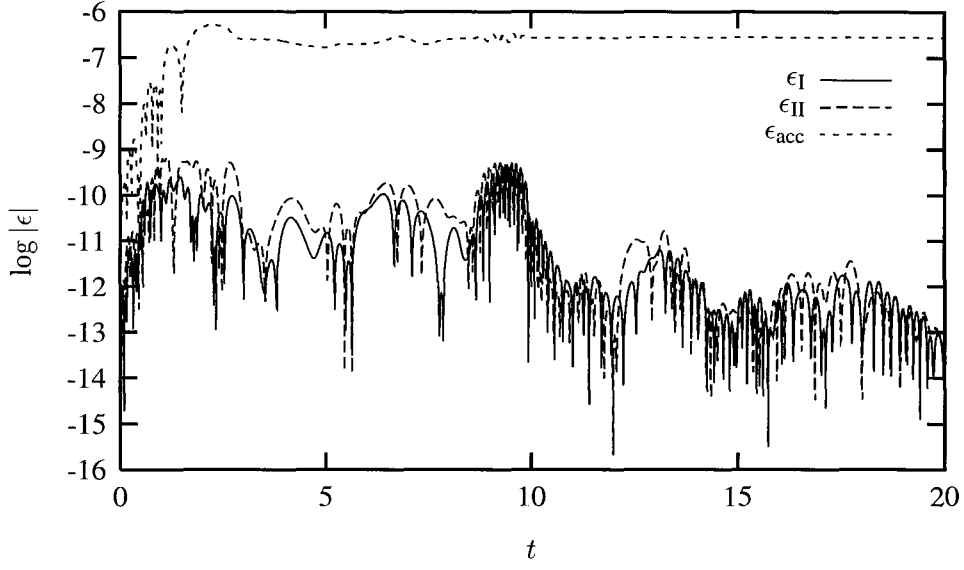[5]The errors are scaled with the total mass.

Figure 4.6: The relative errors in the conservation of mass. Re $= 2500$, Pe $= 5000$ and $N = M = 120$.

form Eq. (4.9) results in an expression for the loss of mass during a single time step. Since these separate errors accumulate, the total loss of mass defined as

$$\epsilon_{\text{acc}} = \sum_{\substack{k=0 \\ k \text{ even}}}^{N} \sum_{\substack{l=0 \\ l \text{ even}}}^{M} \frac{\hat{c}_{kl}^{n+1} - \hat{c}_{kl}^{0}}{(k^2 - 1)(l^2 - 1)}, \tag{4.10}$$

is a few orders of magnitude larger than the separate errors (see Figure 4.6). At lower Reynolds and Peclet numbers the solution is more smooth, resulting in smaller errors at the same number of Chebyshev modes.
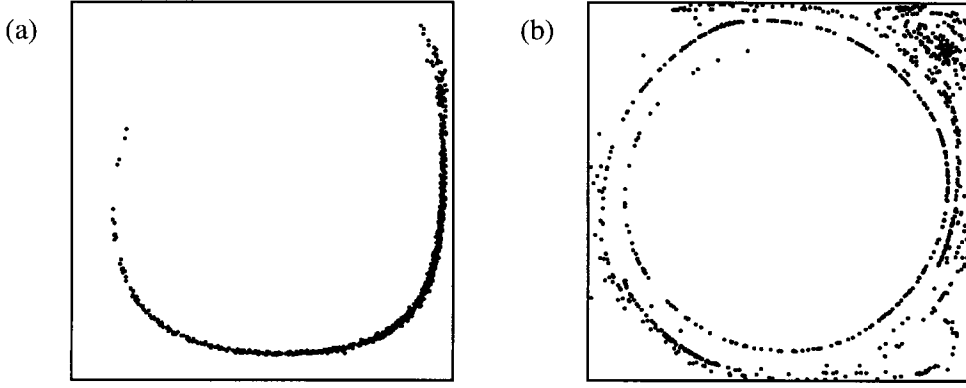
Figure 4.7: Particle distribution during spin-up at $t = 20$ for Re $= 100$ (a) and Re $= 1000$ (b).

4.2.2 Lagrangian approach

In order to test the numerical algorithm for the Lagrangian method, simulations of spin-up are performed with Re $= 100$ and Re $= 1000$. Similar to the procedure as described in the previous section, we start the simulation of tracer trajectories at $t = 2$. The initial tracer distribution consists of 1000 random points Gaussianly distributed around $(x, y) = (0.7, 0.7)$ with variance 0.1. The particle paths are integrated with time step $\Delta t = 5 \times 10^{-4}$ up to $t = 20$. First we show the results of the simulations performed without the random walk method, then we will discuss the results of simulations with tracer diffusion.

The particle distributions at $t = 20$ are shown in Figure 4.7 for both Re $= 100$ and Re $= 1000$. For Re $= 100$ the cloud of particles is elongated along the stream lines, and since the stream function is quasi-stable, hardly any mixing takes place. For Re $= 1000$ a large amount of particles is captured in the secondary cell, which occurs in the upper right corner of the container. The tracers outside the corner cell are drawn into a spiral structure by the core vortex.

In order to estimate the accuracy of the algorithm, these simulations are performed with a different number of Chebyshev polynomials, as well. The mean difference in the position of the tracers is defined as

$$\epsilon_{\mathbf{x}} = \frac{1}{N_p} \sum_{i=1}^{N_p} |\mathbf{x}_i^{N_{\max}} - \mathbf{x}_i^{N}|, \qquad (4.11)$$

where the $\mathbf{x}_i^{N}$ denotes the position of the i-th particle calculated using N Chebyshev modes. The maximum number of Chebyshev polynomials used for the approximation of the velocity field $N_{\max}$ is 80 for Re $= 100$ and 120 for Re $= 1000$. The time-evolution of $\epsilon_{\mathbf{x}}$ is displayed in Figure 4.8 for Re $= 100$ and in Figure 4.9 for Re $= 1000$. The substantial increase of the deviation during the initial stage ($t < 3$) originates from the difference in the velocity fields. Since the error in the velocity fields increases for smaller N, the deviation of the particle positions also increases for smaller N. After the initial stage the difference grows linearly in time for Re $= 100$. At higher Reynolds numbers the flow becomes unsteady, introducing chaotic particle motion. Chaotic advection implies that the paths followed by two particles that are separated by an infinitesimal distance will tend to diverge exponentially.
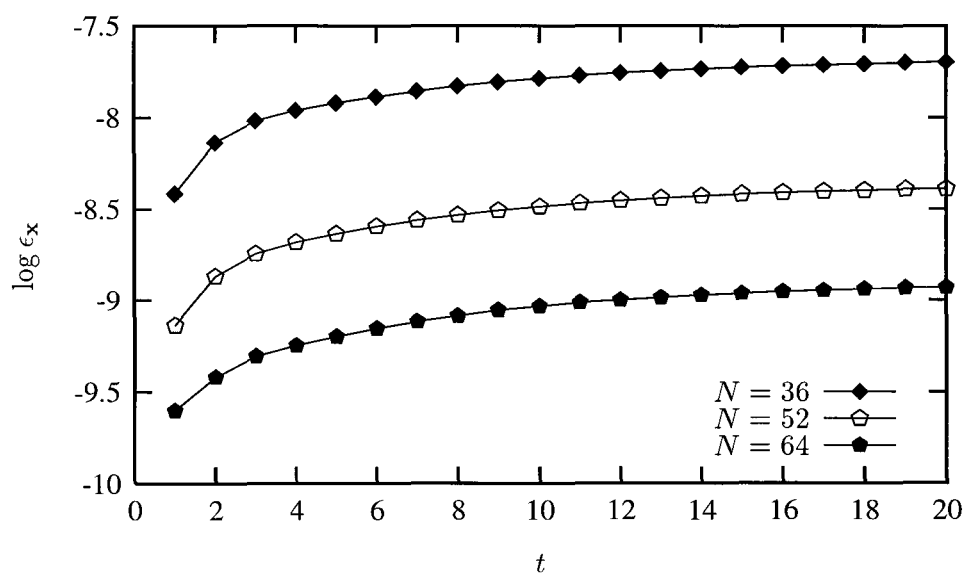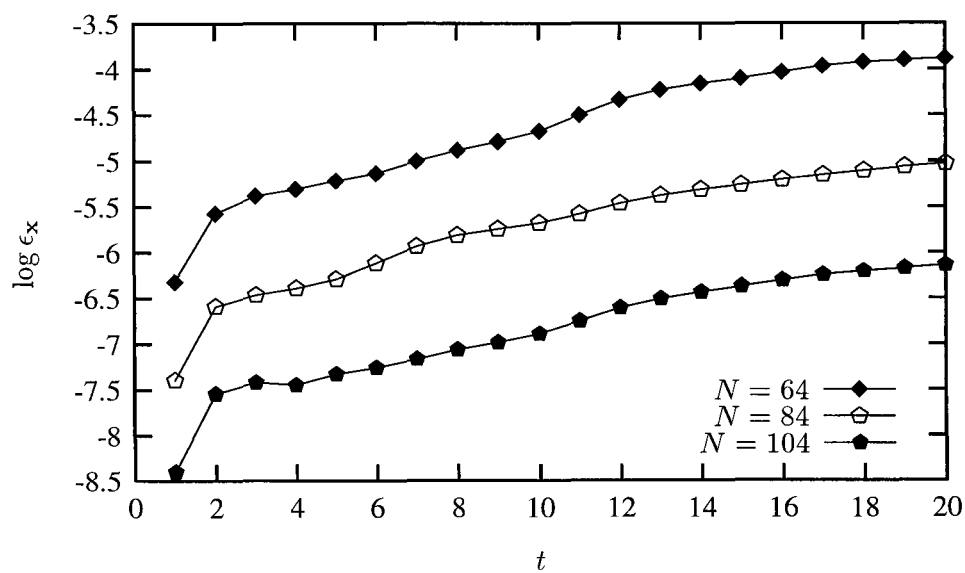
Figure 4.8: Time-evolution of ϵ_x for Re $= 100$.

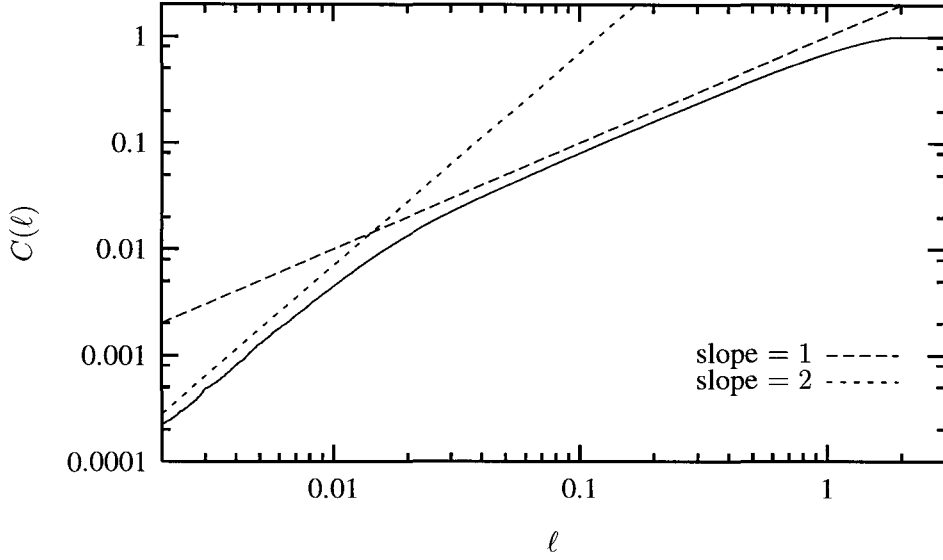**Figure 4.9:** Time-evolution of ϵ_x for Re $= 1000$.

Figure 4.10: Correlation integral of the distribution displayed in Figure 4.7(a). ($t = 20$)

This exponential behaviour can clearly be seen in Figure 4.9. The same series of simulations but with a smaller time-integration step does not yield significant smaller differences.

In Section 3.3.2 we have introduced the correlation integral $C(\ell)$ for the characterization of the degree of mixedness. In order to elucidate this method, the correlation integral of the tracer distributions displayed in Figure 4.7 are shown in Figure 4.10 and 4.11. Note that $C(\ell)$ is normalized with the total number of pairs $[N_p(N_p - 1)/2]$. First consider the curve corresponding to the tracer distribution for Re $= 100$. In the range $\ell \lesssim 0.02$ the correlation integral behaves like $C(\ell) \sim \ell^2$ which corresponds to a homogeneous distribution of the tracers within the elongated blob. The position of the bend in the curve ($\ell \approx 0.02$) corresponds to the thickness of the filament. At larger scales ($0.02 \lesssim \ell \lesssim 2$) the tracer distribution can be considered as a single well-separated filament. Therefore the correlation exponent equals one in this subrange. The correlation integral of the distribution which has been computed with Re $= 1000$, exhibits a large range in which $C(\ell) \sim \ell^\mu$, with $\mu = 1.36 \pm 0.01$, which corresponds to thin separated filaments of tracer. The distance at which $C(\ell)$ begins to flatten is indicative of the overall extent of the cloud. In this case both correlation integrals reach the maximum value of 1 at $\ell \approx 2$.

Calculations of spin-up for Re $= 1000$ have also been performed using the random-walk method to simulate tracer diffusion. The Peclet number was set to 10000 and the initial conditions as before. We have used 64 and 84 Chebyshev polynomials to approximate the velocity field. Figure 4.12 shows the time-evolution of the variance of the tracer distribution for both simulations. The relatively large difference between the two curves (a few percent) is due to the slow convergence of the random-walk method. In order to reach an accuracy comparable to the accuracy of the Eulerian approach order $\mathcal{O}(10^{10})$ particles are needed. This is far beyond our current computational resources; a comparable simulation with $\mathcal{O}(10^{10})$ particles would take thousands of years. However, it is not hard to realize that the Lagrangian
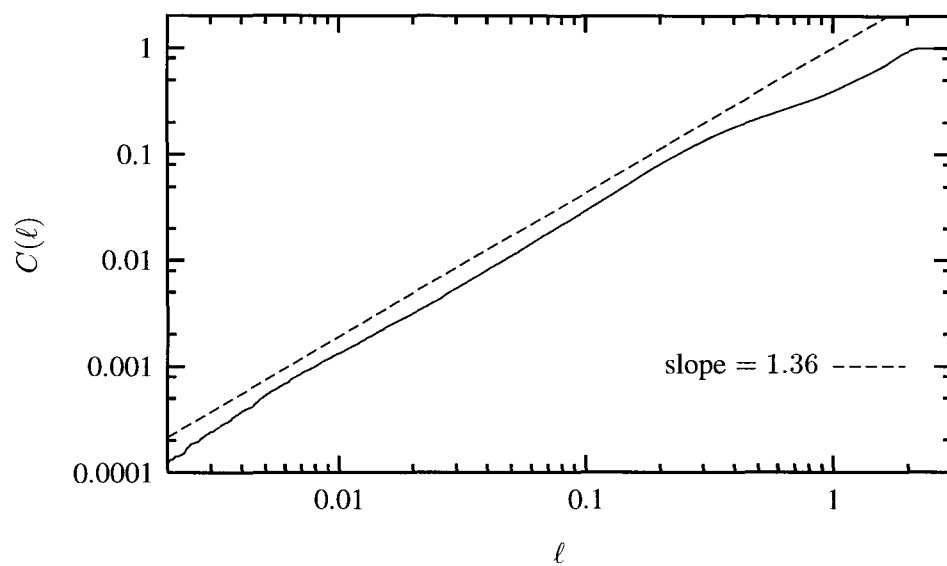
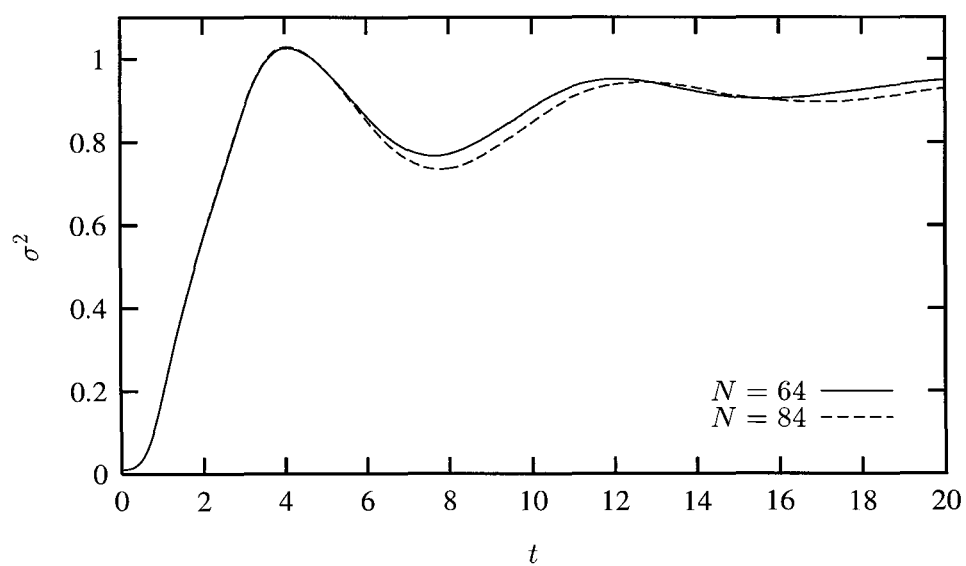**Figure 4.11:** Correlation integral of the distribution displayed in Figure 4.7(b). ($t = 20$)

Figure 4.12: Time-evolution of σ^2 during spin-up with Re $= 1000$ and Pe $= 10000$.

approach is ideally suited for parallel computation and an implementation of the method on a parallel computer reduces the computation time by an order of magnitude.

4.3   Linear Array of Vortices

Our main objective of the development of numerical algorithms to simulate the advection of passive tracers in 2D-flows is to investigate chaotic advection in a linear array of vortices. The transport process in such a cellular flow can be considered as a one-dimensional model for mixing in turbulent flows. An example of cellular flow is Rayleigh-Bénard convection which occurs in a fluid layer which is confined between two horizontal planes and is heated from below. A cellular pattern can also arise due to self-organization in 2D-flow. The so-called inverse energy cascade, according to which kinetic energy shows a spectral flux to the larger scales of motion, results in the formation of larger, organized coherent flow structures. Experiments on the self-organization of flows in stratified fluids in rectangular containers are described by Flór [34]. In his experiments a flow was generated by either using two horizontal jets in juxtaposition at the longer sidewalls or by stirring the fluid in the entire domain with a rake. In both types of experiments the flow becomes organized in a cellular pattern.

Spin-up experiments on fluid in a rectangular container reported by van Heijst, Davies & Davis [29] also revealed the self-organization of the flow in an array of quasi-2D cells, with the number of cells roughly scaling with the aspect ratio of the container. During the initial stage of spin-up the cyclonic vorticity, generated in the boundary layers, will be convected by the primary anticyclonic cell along the sides of the container. In the subsequent stage it is observed that the advected cyclonic vorticity gets accumulated in cyclonic cells in the corners of the domain, with the cells at the downstream ends of the longer side walls being larger and more intense than those in the corners downstream of the shorter walls. The larger cells then grow and migrate into the interior, upon which complicated, irregular flow patterns may be observed. The details of the flow evolution in this transition stage depend on the rotation parameters and on the aspect ratio $\delta = L/B$, with L and B the length and the width of the tank, respectively. Via a complicated process of interactions between cells the flow is finally observed to organize into an array of counter-rotating cells which completely fills the domain. A quasi-stationary state sets in because the decay of the cells occurs on a time scale considerably larger than the eddy turnover time scale. During this stage the cell positions reveal a small oscillatory motion [33]. The oscillation parallel to the long side walls (x-direction) are approximately in phase, whereas the oscillations perpendicular to the long side walls are out of phase. At the same time the strength of the vortices reveals an oscillation as well. This phenomenon is also observed in Rayleigh-Bénard convection and in the experiments presented by Flór [34].

We have simulated the advection of a passive tracer in an array of vortices which originates from self-organization during spin-up. The results of the simulations performed in containers with aspect ratio $\delta = 3$ and $\delta = 5$ are presented in the following sections.

4.3.1   Aspect ratio 3

The size of the container has been made dimensionless using the half width of the container, i.e., the Reynolds number is defined by Re $= \Delta\Omega B^2/4\nu$. It also implies that for aspect ratio 3 the dimensionless domain is given by $[-3, 3] \times [-1, 1]$.

We have simulated spin-up at Re $= 1250$ without tracer, until an array of vortices exists. At $t = 25$, when three counter-rotating cells can be observed, the time is reset to zero and the tracer is added. The initial tracer distribution consists of a Gaussian "hill" with an e-folding value of 0.5, which is placed at the left side of the domain:

$$c(x, y, 0) = c_{\text{max}} \exp \left[- \left(\frac{x + \delta}{0.5} \right)^2 \right].$$ (4.12)

The maximum value of the tracer distribution denoted by c_{max}, has been chosen in such way that the total dimensionless concentration is approximately one.

Two simulations have been performed in the Eulerian approach with different Schmidt numbers: Sc $=$ Pe/Re $= 1$ and Sc $= 4$. The simulation results with Sc $= 1$ has been obtained with $N = 120$ and $M = 64$ while the simulation with Sc $= 4$ has been based on a computation with $N = 160$ and $M = 80$. The time step is in both cases $\Delta t = 5 \times 10^{-4}$. Although this time step does not satisfy the stability restriction $\Delta t \leq 9/N^2$, the simulations appeared to be stable. Figure 4.13 shows a sequence of snapshots of the tracer distribution during the simulation with Sc $= 4$. At $t = 5$ the initial distribution has been drawn into a spiral structure by the left vortex. From then the tracer is pulled into the central cell near the oscillating stagnation point at the upper wall between the two left cells ($10 \lesssim t \lesssim 100$). From $t = 20$ the tracer enters the right cell in the same way, now near the stagnation point at the bottom wall between the right and central cell. At $t = 150$ the tracer has been distributed homogeneously in the outside of each cell, whereas the core of the vortices has not been penetrated yet. At this time the oscillation of the cells has almost disappeared and the total dimensionless energy of the flow defined as $\frac{1}{2} \iint (u^2 + v^2) dA$, has decreased to approximately 10% of its value when the tracer was added. Therefore the inter-cellular flux of tracer is now mainly due to diffusion instead of chaotic advection. The simulation with Sc $= 1$ results in nearly the same concentration fields, with the exception that thin filaments are spread due to diffusion.

Simulations of the advection of particles based on the Lagrangian approach have been performed in the same flow. The initial positions of the particles form two Gaussian blobs with an e-folding value of 0.1 placed at $(x, y) = (-2.8, 0)$ and $(-2, -0.5)$. The particle distribution at several times are shown in Figure 4.14. The blob which initially was placed in the core of the left cell, has been stretched out and rolled up, but not a single particle has left the cell. However, the other blob, originally placed near the middle of the left wall, has entered the central and right cell. Note the striking resemblance of some features of the continuous and the particle distribution at $t = 20$: a single filament entering the right cell and the characteristic folding near the stagnation point at the upper wall.

The dispersion of a passive tracer can be characterized by the variance of the tracer cloud about its mean position. Since we are interested in the diffusion in only one direction, we introduce the variance in one dimension (x) with respect to the left wall of the container:

$$\sigma_x^2 = \frac{\iint (x + \delta)^2 c(x, y) dA}{\iint c(x, y) dA}.$$ (4.13)

Figure 4.15 represents, on a log–log plot, the evolution of σ_x^2 as a function of time. The plot displays
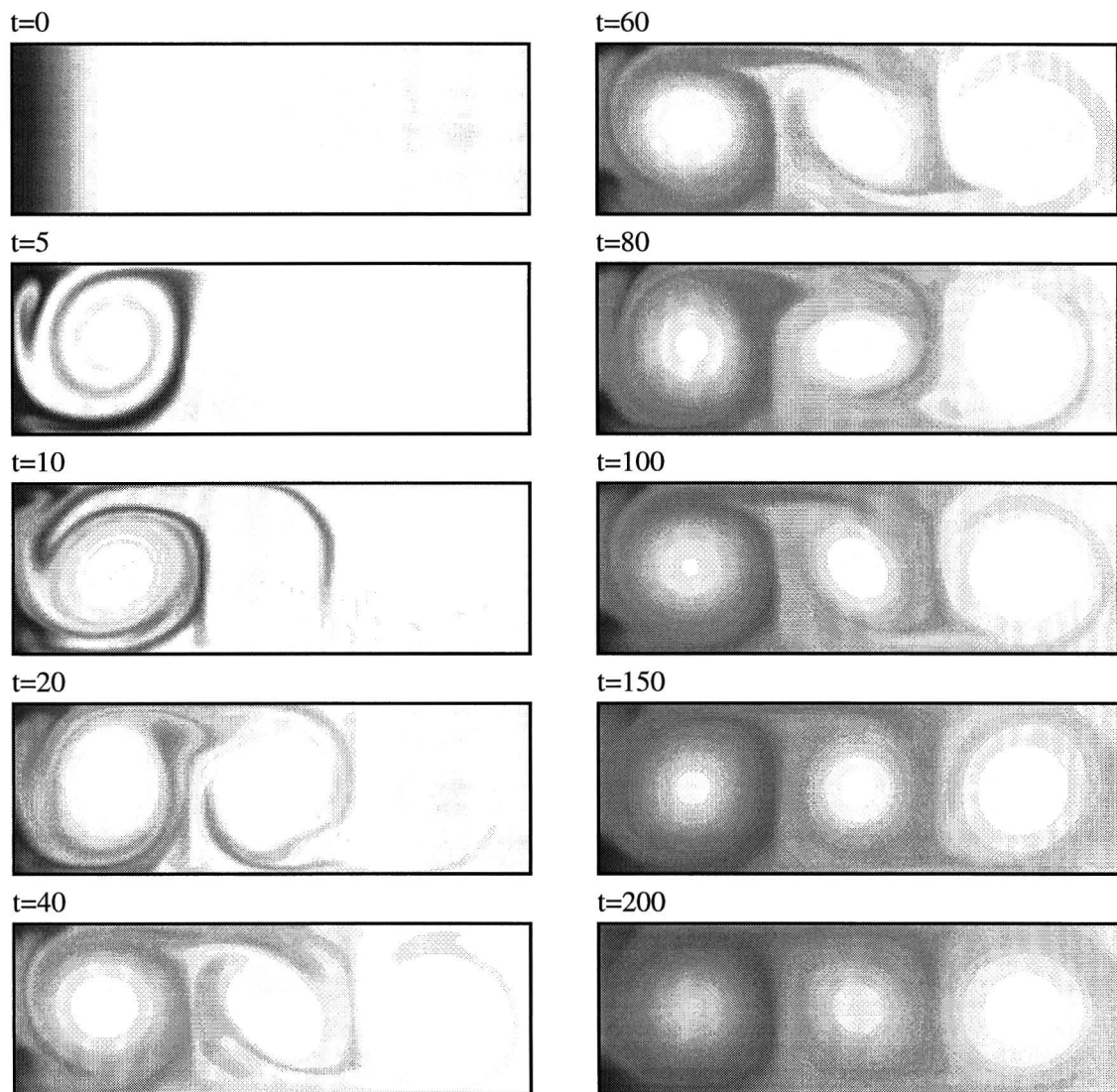
t=0

t=60

t=5

t=80

t=10

t=100

t=20

t=150

t=40

t=200

Figure 4.13: Snapshots of the tracer distribution, $\delta = 3$, Re $= 1250$ and Sc $= 4$.
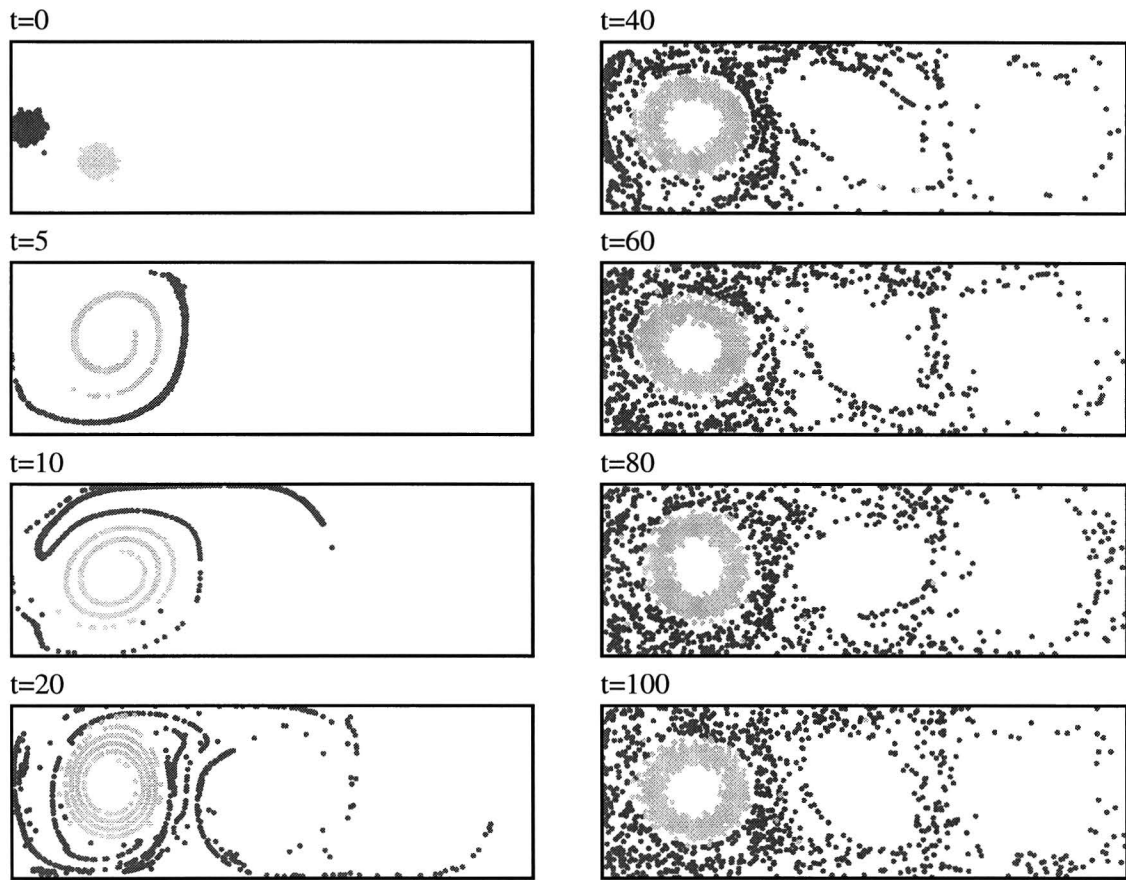
Figure 4.14: Snapshots of the particle distribution, $\delta = 3$ and Re $= 1250$.

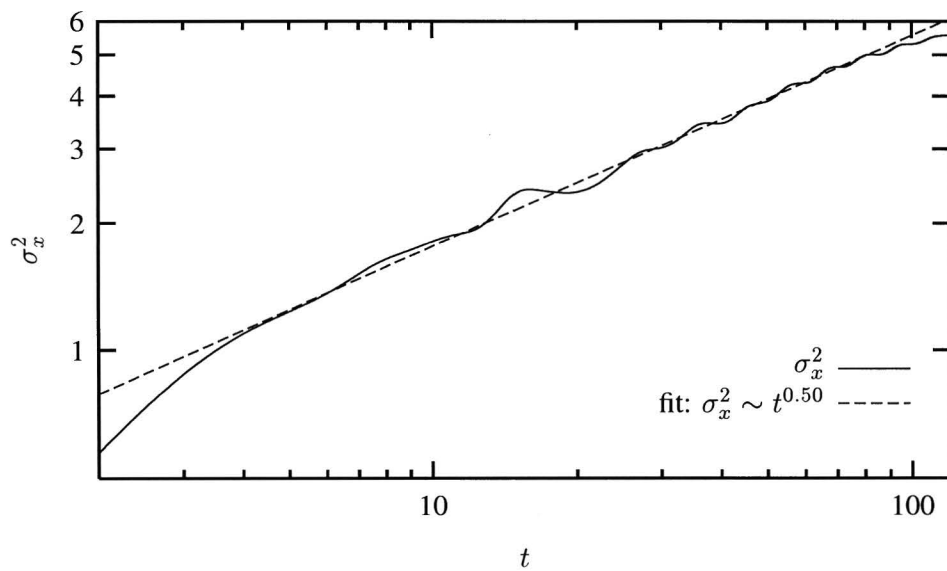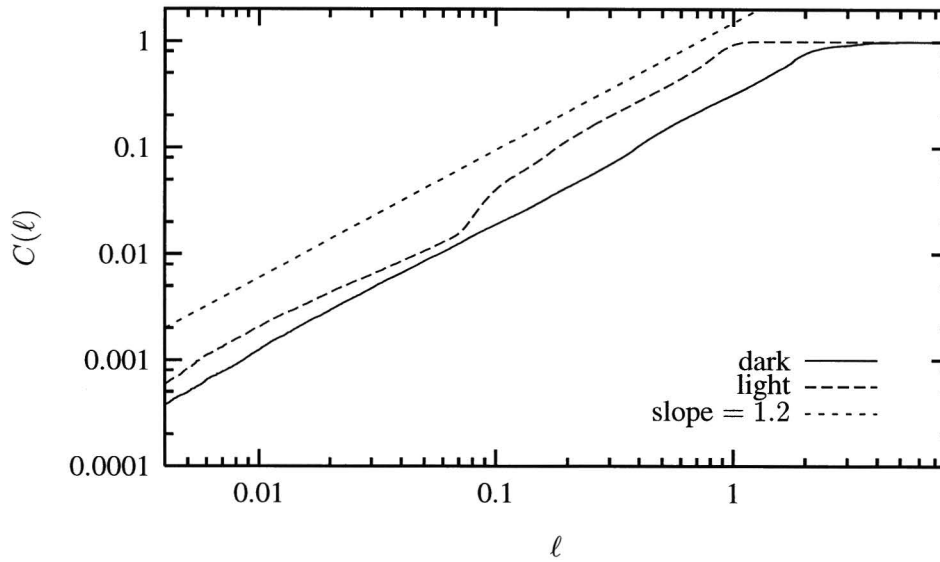**Figure 4.15:** Time-evolution of σ_x^2 with $\delta = 3$, Re $= 1250$ and Sc $= 4$.

Figure 4.16: Correlation integral of the particle distributions displayed in Figure 4.14. The solid curve represents the dark particles, whereas the dashed curve represents the light particles. The small-dashed line is a guide to the eye with slope 1.2.

a power law with the following exponent: $\sigma_x^2 \sim t^\alpha$, with $\alpha = 0.50 \pm 0.01$. The dispersive process is thus, according to the value of the exponent, slower than normal dispersion, where $\alpha = 1$; it can therefore be termed as hypodiffusive.[6] For increasing t the slope of the curve decreases. This is due to the decay of the flow, which reduces the inter-cellular transport of the tracer. The curve exhibits a small oscillation with a period that corresponds to the eddy turnover time (the period that a particle needs to complete one turnover).

Figure 4.16 displays, on a log–log plot, the correlation integral for both particle distributions shown in Figure 4.14 as a function of ℓ. The curve representing the light particles shows two ranges in which the slope of the curve is approximately 1.2. These two ranges are separated by a bend at $\ell \approx 0.1$ which corresponds to the distance between the filaments. The curve reaches its maximum value at $\ell \approx 1$, which implies that the overall extent of the particle distribution is smaller than one cell. The correlation integral of the dark particles exhibits a large range where $C(\ell) \sim \ell^\mu$ with $\mu = 1.20 \pm 0.01$. This indicates that the tracer is not at all well mixed; well-separated filaments are still apparent. The maximum value of 1 is reached at $\ell \approx 5$, which indicates that the particles have been distributed throughout the whole domain.

4.3.2 Aspect ratio 5

We consider spin-up in a container with aspect ratio 5 for two different Reynolds numbers: Re $= 625$ and Re $= 1250$. In both cases a cellular pattern has been formed at $t = 50$. However, a striking

---

[6]The term hypodiffusion may sound confusing, since the dispersion process is actually much faster than molecular diffusion.

difference is the number of cells; for Re $= 625$ there exist 5 cells, whereas 7 cells are present for Re $= 1250$. Moreover, the flow pattern at Re $= 1250$ is seen to be less stationary and the strength of the vortices is very different.

At $t = 50$ the simulation of the advection of the passive tracer is started. The initial tracer distribution equals the distribution given by Eq. (4.12) and the Peclet number is in both cases 1250, i.e. Sc $= 1$ for Re $= 1250$ and Sc $= 2$ for Re $= 625$. Both simulations have been performed with $N = 180$ and $M = 60$, and the time-integration step $\Delta t = 5 \times 10^{-4}$.

Figure 4.17 shows the results of the simulation with Re $= 1250$ by means of concentration plots at several times. In Figure 4.18 the stream function plots are displayed. The initial distribution is rolled up by the first roll like we have seen for $\delta = 3$. However, in this case the left vortex is anticyclonic, whereas for $\delta = 3$ the first cell is cyclonic. Therefore the exchange of tracer between the first two cells occurs in this case near the stagnation point at the bottom wall. At $t = 25$ it is seen that the tracer enters the third cell and at $t = 50$ the tracer has reached the central cell. Since the velocity of the fluid in this case is much smaller than the velocity for $\delta = 3$, the effective diffusion is larger. This causes the cells to be filled with tracer in a relative short time. At $t = 150$ the fluid is nearly motionless and the simulation is discontinued.

For Re $= 625$ the velocity in the cellular pattern is even smaller and the decay of the vortices is faster. Therefore the fluid is practically motionless at $t = 100$. At this moment the tracer has not entered the third cell, while the first cell is almost homogeneously filled. The tracer distribution at $t = 100$ is shown in Figure 4.19.

The dispersion of the tracer distribution is characterized by the one-dimensional variance defined by Eq. (4.13). The time-evolution of σ_x^2 is shown in Figure 4.20 for the simulation with Re $= 1250$. The plot displays a power law $\sigma_x^2 \sim t^\alpha$, with exponent $\alpha = 0.60 \pm 0.01$. Again the curve reveals an oscillation with a period corresponding to the eddy turnover time. Like in the case $\delta = 3$, the slope of the curve decreases when time increases. In Figure 4.21 the time-evolution of σ_x^2 is shown for the simulation with Re $= 625$. In this case only one oscillation period is present, which corresponds to the advection of a filament around the first cell. In the range $20 \lesssim t \lesssim 70$ the plot reveals a power law with exponent $\alpha = 0.50 \pm 0.01$. At larger times the slope of the log–log plot decreases due to the decay of the flow.

For all our simulations we have found an exponent smaller than 1, which indicates that the dispersion of a passive tracer in an array of vortices is a hypodiffusion process. The simulation with $\delta = 5$ and Re $= 1250$ reveals an exponent which is slightly larger than the others ($\alpha = 0.60$ and $\alpha = 0.50$, respectively). This is probably due to the relatively strong motion of the cells in the former case, which causes a better exchange of tracer between the cells. Although the exponent derived by Guyon *et al.* [20] is based on a time-independent cellular flow, the present results show some striking resemblance. Moreover, it must be noted that the particular value of $\alpha = 0.5$ is a special case of anomalous diffusion (see Young [35]).
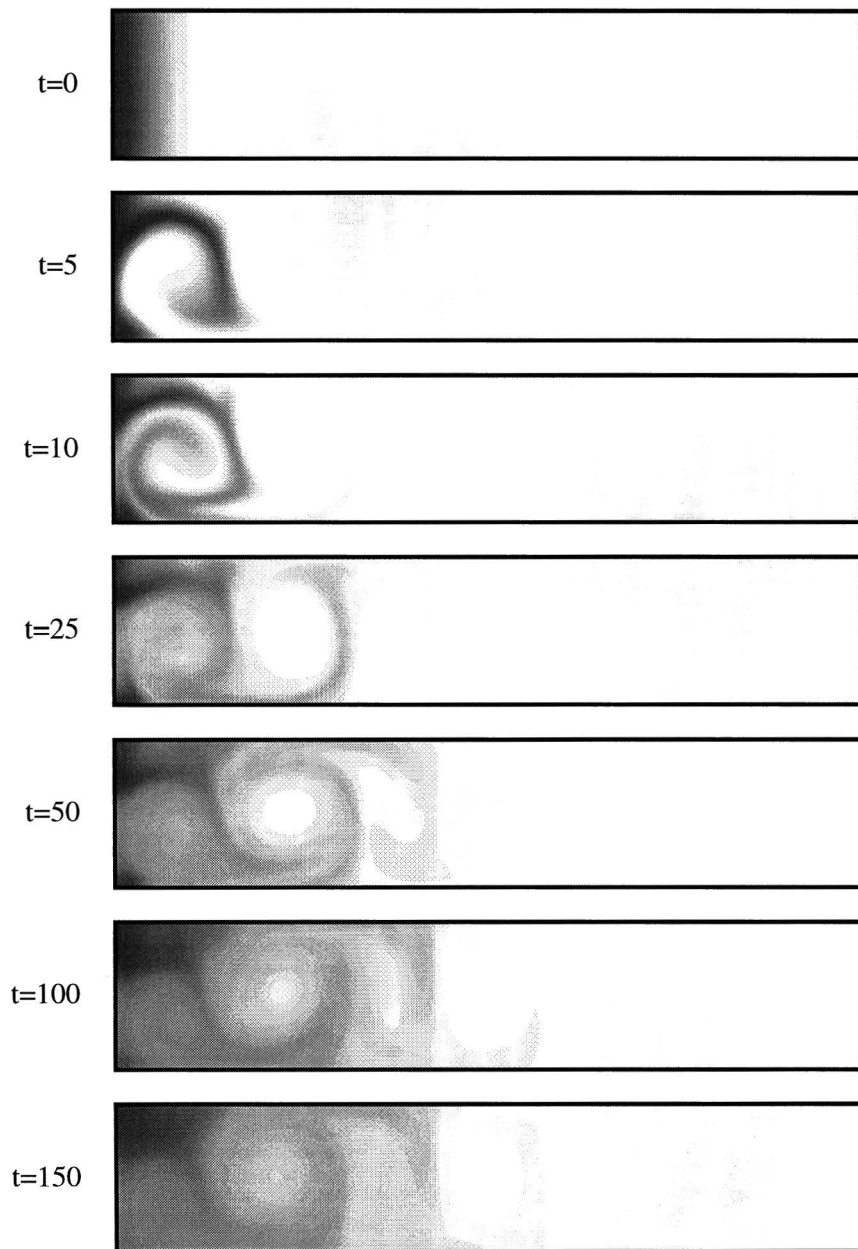
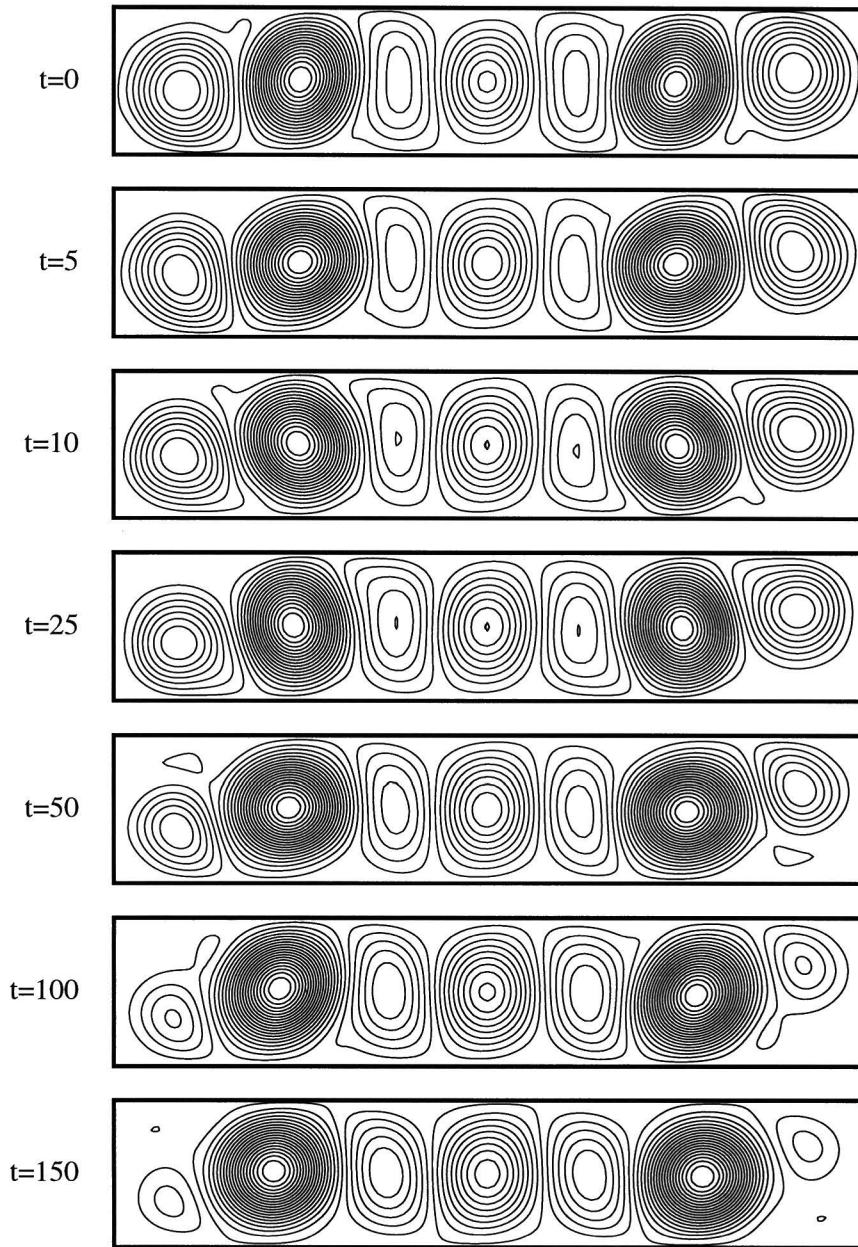**Figure 4.17:** Snapshots of the tracer distribution, $\delta = 5$, $\mathrm{Re} = 1250$ and $\mathrm{Sc} = 1$.

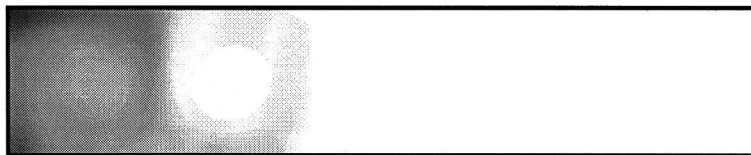**Figure 4.18:** Stream function, $\delta = 5$ and Re $= 1250$.

Figure 4.19: Tracer distribution at $t = 100$, $\delta = 5$, Re $= 625$ and Sc $= 2$.

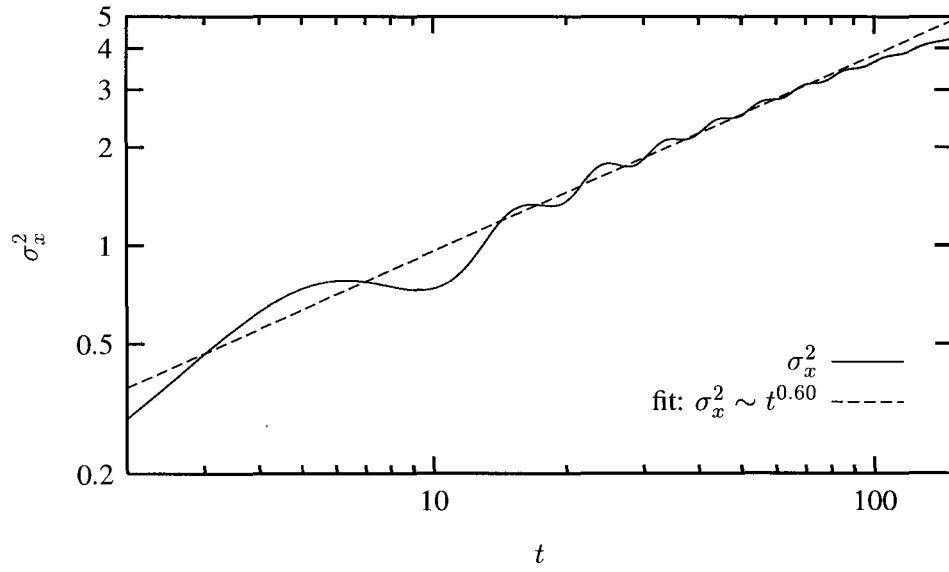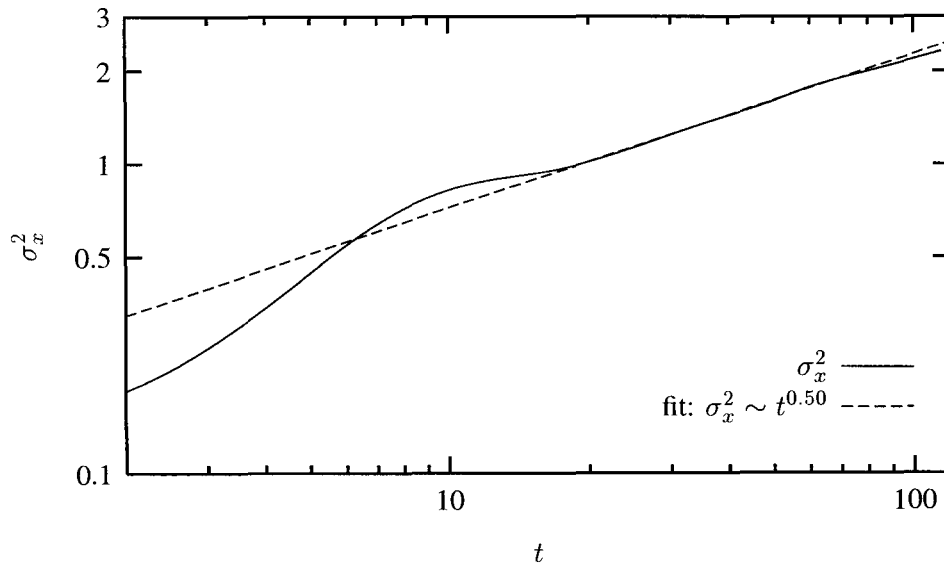**Figure 4.20:** Time-evolution of σ_x^2 with $\delta = 5$, Re $= 1250$ and Sc $= 1$.

Figure 4.21: Time-evolution of σ_x^2 with $\delta = 5$, Re $= 625$ and Sc $= 2$.

Chapter 5

Conclusions

In this report we have discussed the numerical simulation of passive tracers in 2D flow. The 2D Navier-Stokes equations are solved in velocity-vorticity formulation using a pseudospectral method based on the expansion of the flow variables in series of Chebyshev polynomials. We have used a spectral solver for flows with two nonperiodic directions, which has been developed by Clercx [4]. The boundary condition for the vorticity and the requirement that the flow should be divergence-free are enforced with an influence matrix including a tau-correction procedure.

For the simulations of passive tracers two numerical methods have been developed. In the first method, based on the Eulerian approach, the transport of a passive scalar field is expressed by the advection-diffusion equation. Time discretization results in a Helmholtz equation with homogeneous Neumann boundary conditions, which is solved using a Chebyshev tau method. The second method, known as the Lagrangian approach, consists of following a large amount of passive particles. The trajectory of a particle is determined by integration of the velocity of the tracer, which is computed by a direct transformation from spectral to physical space. The effect of diffusion is simulated by a random-walk method which uses a Lagrangian approach based on the stochastic differential corresponding to the scalar advection-diffusion equation.

Simulations of natural convection in a square cavity are performed in order to test the numerical algorithm designed for the integration of the Navier-Stokes equations and the implementation of the numerical scheme for the integration of the advection-diffusion equation. Comparison of the results with data from the literature is satisfactory; the benchmark data of De Vahl Davis [28] and Le Quéré [27] could be reproduced very well.

In order to test both numerical algorithms — the Eulerian and the Lagrangian approach — simulations of passive tracers in spin-up have been performed. The accuracy of the results appeared to be very dependent on the accuracy of the velocity field. The simulations also revealed that a large number of Chebyshev modes is needed to resolve the steep gradients in the concentration fields, which occur at high Peclet numbers. Simulation of diffusion in the Lagrangian approach proved to be very impractical due to the slow convergence of the random-walk method. Summarizing we can conclude that the

Eulerian approach is suitable for simulations involving relatively small Peclet numbers (Pe $\lesssim 10^5$), whereas the Lagrangian approach is practical for the simulation of non-diffusive tracers.

The developed methods have been applied for the investigation of transport of a passive tracer in a linear array of vortices, which originates from the self-organization during spin-up in a rectangular container. The wiggling of the cells during the quasi-steady state introduces chaotic advection, like it has been observed in the experiments by Flór [34]. The dispersion of the tracer in this cellular flow appeared to be a hypodiffusive process, where the variance of the tracer cloud behaves like $\sigma_x^2 \sim t^\alpha$, with α close to 0.5. Due to viscosity the velocity of the fluid decays, which makes this flow unsuitable for the study of chaotic advection and anomalous diffusion in a cellular flow. Hence, we recommend to simulate the advection of a passive tracer in a flow which is forced by, for example, moving boundaries or an external force. Depending on the Reynolds number we expect to be able to distinguish several regimes in such a forced flow: steady, periodic, chaotic and turbulent flow. The investigation of the transport properties of these flows could be the goal of future studies.

The numerical algorithm based on the Eulerian approach does not satisfy the conservation of mass within machine accuracy. The very small errors which occur at every time step are explained and therefore we expect that with some further attention this problem will be solved.

Since both methods to simulate passive tracers can be easily extended to three dimensions, they can be used for the investigation of mixing in three dimensional configurations as well.

References

[1] H. AREF, Stirring by chaotic advection, J. Fluid Mech. **143**, 1 (1984).

[2] R. T. PIERREHUMBERT, Large-scale horizontal mixing in planetary atmospheres, Phys. Fluids A **3**, 1250 (1991).

[3] T. H. SOLOMON & J. P. GOLLUB, Chaotic particle transport in time-dependent Rayleigh-Bénard convection, Phys. Rev. A **38**, 6280 (1988).

[4] H. J. H. CLERCX, A spectral solver for the Navier-Stokes equations in the velocity-vorticity formulation for flows with two nonperiodic directions, Submitted to J. Comp. Phys. (1996).

[5] K. J. RICHARDS, Y. JIA & C. F. ROGERS, Dispersion of tracers by ocean gyres, J. Phys. Oceanogr. **25**, 873 (1995).

[6] L. KLEISER & U. SCHUMANN, Treatment of incompressibility and boundary conditions in 3D numerical spectral simulations of plane channel flow, in *Proceedings Thrid GAMM-conference on Numerical Methods in Fluid Mechanics*, edited by E. H. Hirschel, page 165, Vieweg, Braunschweig, 1980.

[7] H. D. NGUYEN, S. PAIK & J. N. CHUNG, Application of vorticity integral conditioning to Chebyshev pseudospectral formulation for the Navier-Stokes equations, J. Comp. Phys. **106**, 115 (1993).

[8] O. DAUBE, Resolution of the 2D Navier-Stokes equations in velocity-vorticity form by means of an influence matrix technique, J. Comp. Phys. **103**, 402 (1992).

[9] C. CANUTO, M. Y. HUSSAINI, A. QUARTERONI & T. A. ZANG, *Spectral Methods in Fluid Dynamics*, Springer-Verlag, New York, 1988.

[10] M. J. A. WILLEMEN, Spectrale methoden in rechthoekige geometrieën voor simulaties van 2D-stromingen, Master's thesis, Eindhoven University of Technology, 1996.

[11] S. A. ORSZAG, Numerical methods for the simulation of turbulence, Phys. Fluids **12,** Suppl. II, 250 (1969).

[12] D. B. HAIDVOGEL & T. ZANG, The accurate solution of Poisson's equation by expansion in Chebyshev polynomials, J. Comp. Phys. **30**, 167 (1979).

[13] J. WERNE, Incompressibility and no-slip boundaries in the Chebyshev-tau approximation: correction to Kleiser and Schumann's influence-matrix solution, J. Comp. Phys. **120**, 260 (1995).

[14] L. S. TUCKERMAN, Divergence-free velocity fields in nonperiodic geometries, J. Comp. Phys. **80**, 403 (1989).

[15] E. KNOBLOCH & W. J. MERRYFIELD, Enhancement of diffusive transport in oscillatory flows, Astrophysical Journal **401**, 196 (1992).

[16] X. B. XUE & A. V. TANGBORN, Numerical simulations of mixing in a two-dimensional flow with buoyancy, Comp. Fluids **25**, 151 (1996).

[17] P. G. SAFFMAN, A theory of dispersion in porous medium, J. Fluid Mech. **6**, 321 (1959).

[18] A. J. CHORIN & J. E. MARSDEN, *A Mathematical Introduction to Fluid Mechanics*, Springer Verlag, New York, 1979.

[19] W. H. PRESS, B. P. FLANNERY, S. A. TEUKOLSKY & W. T. VETTERLING, *Numerical Recipes*, Cambridge University Press, Cambridge, 1986.

[20] E. GUYON, Y. POMEAU, J. P. HULIN & C. BAUDET, Dispersion in the presence of recirculation zones, Nucl. Phys. B **2**, 271 (1987).

[21] W. YOUNG, A. PUMIR & Y. POMEAU, Anomalous diffusion of tracer in convection rolls, Phys. Fluids A **1**, 462 (1989).

[22] O. CARDOSO & P. TABELING, Anomalous diffusion in a linear array of vortices, Europhys. Lett. **7**, 225 (1988).

[23] O. CARDOSO, B. GLUCKMANN, O. PARCOLLET & P. TABELING, Dispersion in a quasi-two-dimensional-turbulent flow: An experimental study, Phys. Fluids **8**, 209 (1996).

[24] T. H. SOLOMON, E. R. WEEKS & H. L. SWINNEY, Observation of anomalous diffusion and Lévy flights in a two-dimensional rotating flow, Phys. Rev. Lett. **71**, 3975 (1993).

[25] P. GRASSBERGER & I. PROCACCIA, Measuring the strangeness of strange attractors, Phys. Rev. Lett. **50**, 346 (1983).

[26] P. CONSTANTIN & I. PROCACCIA, The geometry of turbulent advection: Sharp estimates of the dimension of level sets, Nonlinearity **7**, 1045 (1994).

[27] P. LE QUÉRÉ, Accurate solutions to the square thermally driven cavity at high Rayleigh number, Comp. Fluids **20**, 29 (1991).

[28] G. DE VAHL DAVIS, Natural convection in a square cavity: a benchmark numerical solution, Int. J. Numer. Meth. Fluids **3**, 249 (1983).

[29] G. J. F. VAN HEIJST, P. A. DAVIES & R. G. DAVIS, Spin-up in a rectangular container, Phys. Fluids A **2**, 150 (1990).

[30] J. A. VAN DE KONIJNENBERG, *Spin-up in non-axisymmetric containers*, PhD thesis, Eindhoven University of Technology, 1995.

[31] Y. K. SUH, Numerical study on two-dimensional spin-up in a rectangle, Phys. Fluids A **6**, 2333 (1994).

[32] J. L. A. VISSERS, De numerieke simulatie van spin-up in een rechthoekige tank, Master's thesis, Eindhoven University of Technology, 1994.

[33] F. J. F. TACKEN, Numerical simulation of 2D flows on a rectangular domain by means of the spectral element method, Master's thesis, Eindhoven University of Technology, 1995.

[34] J. B. FLÓR, *Coherent vortex structures in stratified fluids*, PhD thesis, Eindhoven University of Technology, 1994.

[35] W. R. YOUNG, Arrested shear dispersion and other models of anomalous diffusion, J. Fluid Mech. **193**, 129 (1988).